Journal of Hazardous Materials, 6 (1982) 43—83
Elsevier Scientific Publishing Company, Amsterdam — Printed in The Netherlands

ANALYSIS OF BURRO SERIES 40-m³ LNG SPILL EXPERIMENTS

R.P. KOOPMAN, R.T. CEDERWALL, D.L. ERMAK, H.C. GOLDWIRE, Jr., W.J. HOGAN, J.W. McCLURE, T.G. McRAE, D.L. MORGAN, H.C. RODEAN and J.H. SHINN

Lawrence Livermore National Laboratory, P.O. Box 808, Livermore, CA 94550 (U.S.A.)

(Received October 16, 1981; accepted November 11, 1981)

Summary

The U.S. Department of Energy sponsored a series of nine field experiments (Burro series) conducted jointly in 1980 by the Naval Weapons Center, China Lake, California, and the Lawrence Livermore National Laboratory to determine the transport and dispersion of vapor from spills of liquefied natural gas (LNG) on water. The spill volume ranged from 24 to 39 m³, the spill rate from 11.3 to 18.4 m³/min, the wind speed from 1.8 to 9.1 m/s, and the atmospheric stability from unstable to slightly stable. An extensive array of instrumentation was deployed both upwind and downwind of the spill pond. Wind speed and direction, gas concentration, temperature, humidity, and heat flux from the ground were measured at different distances from the spill point and at different elevations relative to ground level. The wind and gas-concentration data were analyzed to further define the fluid dynamic and thermodynamic processes associated with the dispersion of the gas cloud. Data pertaining to differential boiling of LNG and observed rapid phase-transition explosions were also analyzed.

The principal conclusions are summarized as follows: The turbulent processes in the lower atmospheric boundary layer dominated the transport and dispersion of gas for all experiments except Burro 8. Burro 8 was conducted under very low wind-speed conditions, and the gravity flow of the cold gas displaced the atmospheric flow, causing the wind speed within the cloud to drop essentially to zero. This has profound implications for hazard prediction from large accidental spills. High-frequency (3—5 Hz) gas-concentration measurements indicate that peak concentrations within the flammable limits are common with 10-s-average concentrations above 1%. This implies a larger flammable extent than averaged data or calculations would indicate. Differential boiloff of LNG was observed with resultant enrichment of ethane and propane in the cloud at later times. This ethane-enriched region propagates downwind and represents an additional hazard since it is more easily detonated than the methane-rich region. Energetic rapid phase transition (RPT) explosions, though not expected, did occur under at least two different circumstances during the Burro 6 and 9 tests. These explosions were large enough to damage the facility and raise questions about the coupling of the RPT-produced shock wave into the ethane-rich region of the cloud.

1 Introduction

The Burro series of LNG (liquefied natural gas) spill experiments was performed at the Naval Weapons Center (NWC), China Lake, California, between June 6 and September 17, 1980. These experiments were conducted

0304-3894/82/0000—0000/$02.75

jointly by personnel from NWC and the Lawrence Livermore National Laboratory (LLNL) as part of U.S. Department of Energy (DOE) research into LNG safety. In the first experiment, Burro 1, approximately 35 m^3 of liquefied nitrogen was spilled onto water to develop a fog-correction algorithm for the infra-red gas sensor. In the eight remaining experiments, Burros 2—9, 24 to 39 m^3 of LNG was spilled onto water to measure the dispersion of the LNG vapor cloud in the atmosphere under various conditions. Only Burros 2—9 are considered in this paper, with emphasis on Burros 3, 7, 8 and 9.

A more detailed description of the Burro series is presented in [1], together with an extensive compilation of data. The "Experimental description" section of the present paper is based largely on selected portions of [1] and contains brief descriptions of the test facility, instrumentation, data base, and spill experiments. The remainder of the paper presents observations and analyses of the data obtained in these experiments. Topics discussed include observed interactions of the wind field and gas cloud, LNG vapor dispersion, ground heat transfer, humidity enhancement, differential boiling of LNG, and the rapid phase transitions observed during Burros 6 and 9.

2 Experimental description

2.1 Facility and instrumentation array

Figure 1 is a site plan showing the layout of the facility. The water test basin has an average diameter of 58 m, with an average water level about 1.5 m below the surrounding ground level. The average depth of the water is approximately 1 m. The slopes of all but the south bank have been reduced to about 20% to provide less turbulent wind flow over the water test basin. The terrain immediately downwind of the water test basin rises to a height of about 7 m above the water level at a downwind distance of about 80 m and remains relatively level thereafter. A spill plate, attached to the end of the spill pipe and generally located just below the water surface, is used to direct the downward flow of LNG horizontally out onto the pond surface.

A large array of gas-sensing and wind-measuring instruments was deployed upwind and downwind of the spill site to measure properties of the dispersing gas and the atmosphere into which it was dispersing. A schematic diagram of the array, superimposed on the topography around the spill facility, is shown in Fig. 2. The array centerline was oriented along a bearing of 45° true (N 29°30′E magnetic), which coincides with the prevailing southwesterly wind direction (blowing from 225°) for the summer season.

The large array was composed of three smaller arrays: one array of 2-m-high cup-and-vane anemometers to map the wind field, one three-level array of gas sensors (at 1, 3 and 8 m) to track the cloud, and one three-level ar-

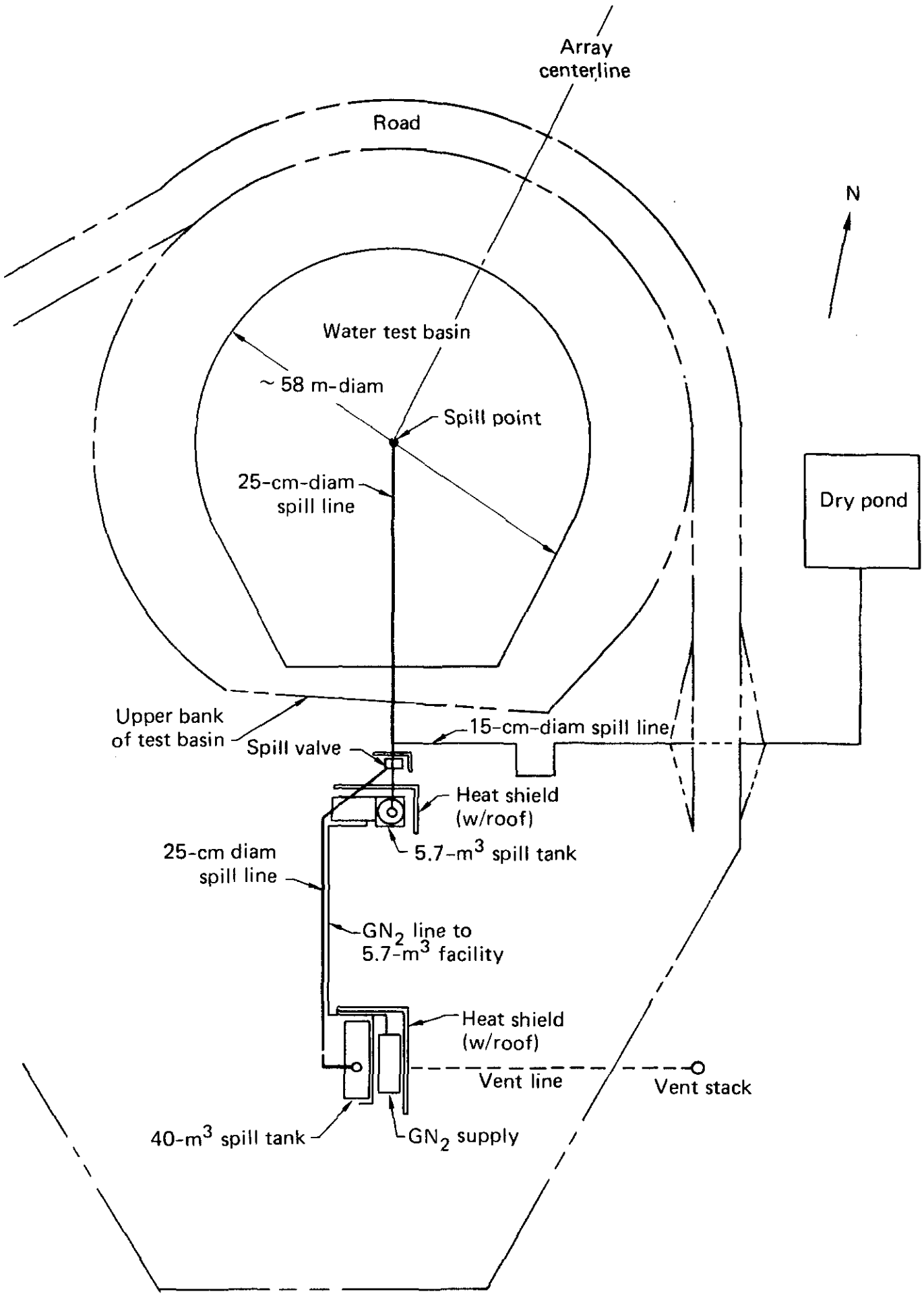

Fig. 1. Site plan of Naval Weapons Center (NWC) spill facility at China Lake.

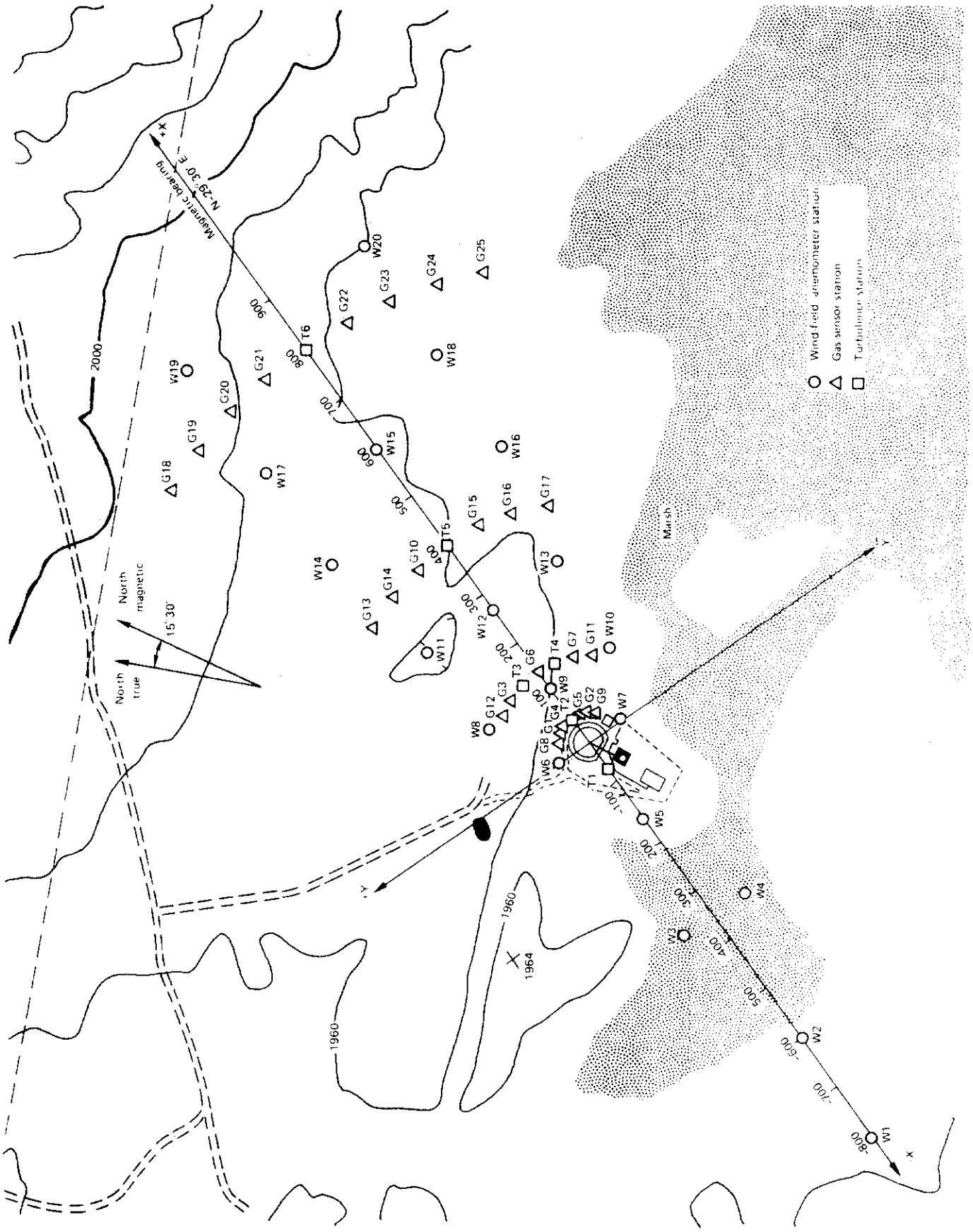

Fig. 2. Instrumentation array for 1980 LNG dispersion tests at the NWC, China Lake.

ray of propeller bivane anemometers (at 1.36, 3 and 8 m) and fast gas sensors (at 1, 3 and 8 m) to track the cloud and measure turbulence effects. A typical turbulence station is shown in Fig. 3. Figure 4 is a photograph looking upwind at the spill facility and the pond between two towers in the 57-m arc.

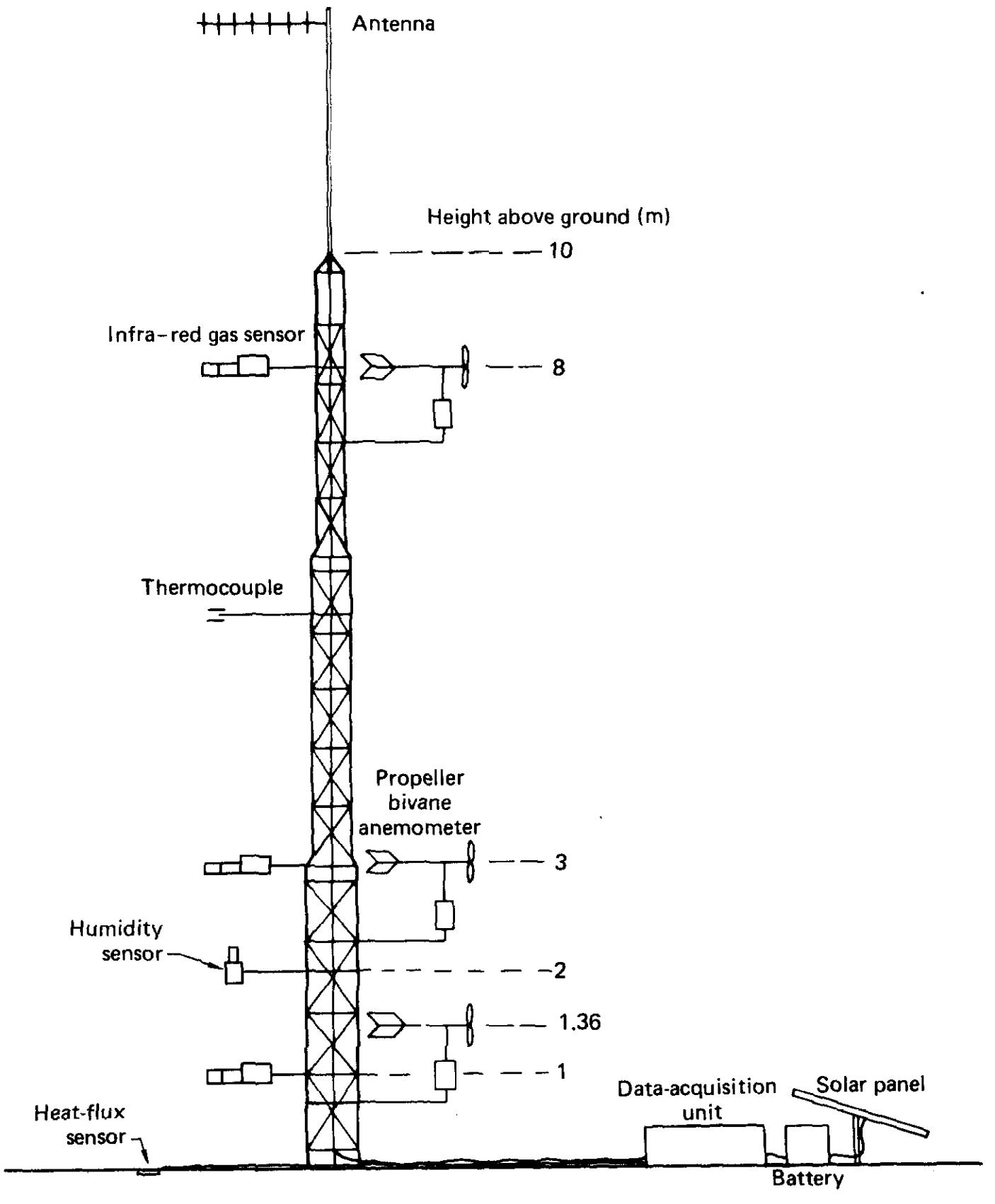

Fig. 3. Typical turbulence station.

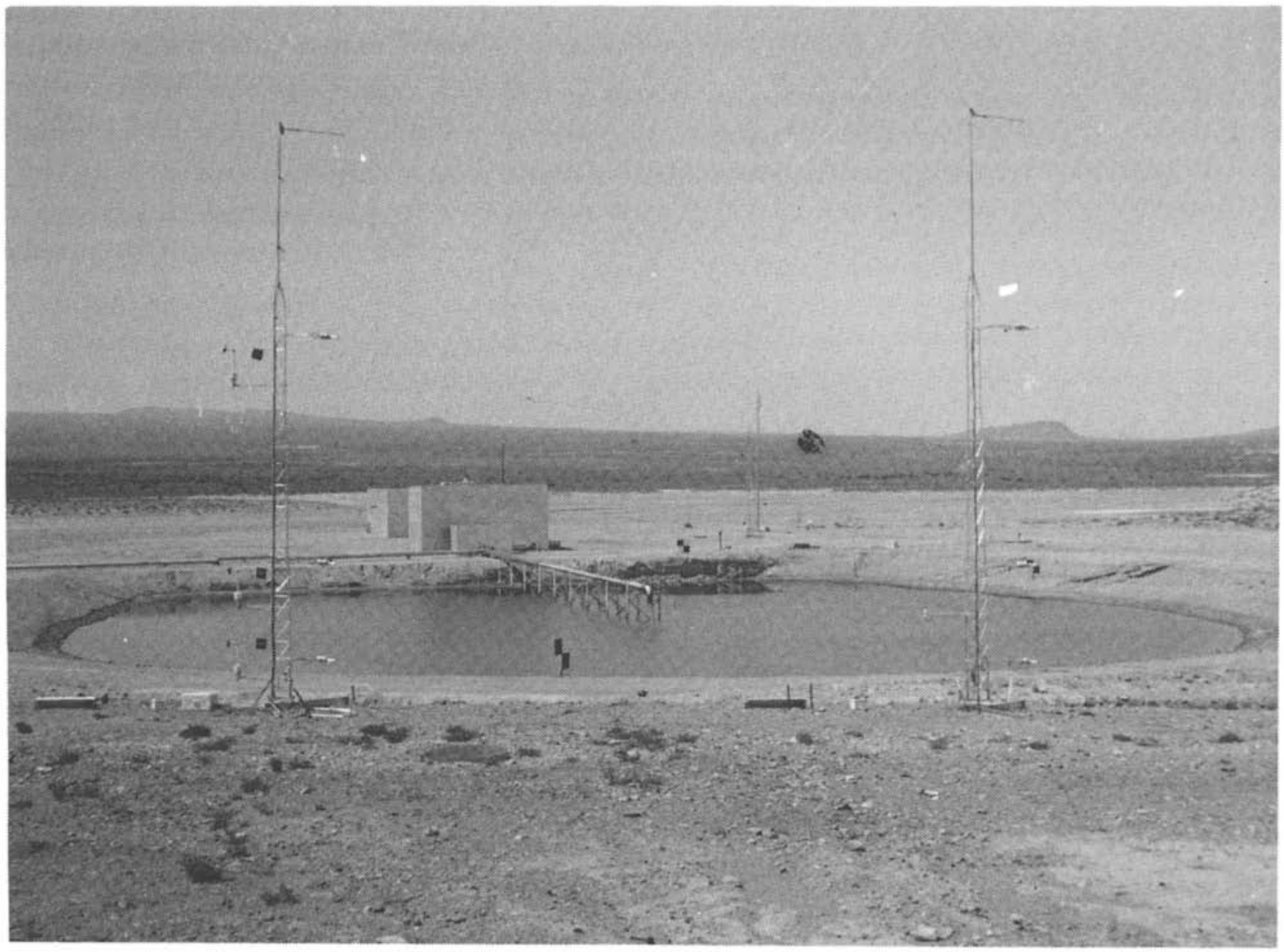

Fig. 4. View of the spill facility and pond, looking upwind between a turbulence station and a gas station in the 57 m arc.

The 20 wind-field stations were located at regular intervals from 800 m upwind to 900 m downwind. The 25 gas stations and 5 turbulence stations were arranged in arcs at 57, 140, 400 and 800 m downwind from the spill point. An additional turbulence station just upwind of the spill pond had bivanes, a humidity sensor and thermocouples, but no gas sensors.

The gas stations were similar to the turbulence stations, except that they had no anemometers. They also took data at a slower rate (1 sample/s, compared to 3 to 5 samples/s for the turbulence stations). Seven of the gas stations had humidity and heat-flux sensors, as well as the normally present gas and temperature sensors. The remaining 18 gas stations had three levels of gas sensors and themocouples.

All of the stations were battery-powered and microprocessor-controlled, with some onboard memory. They communicated with the data-recording trailer by radiotelemetry, turning on instruments on command and sending back data when polled.

2.2 Instrumentation

The instrumentation used in the Burro experiments is described in detail in [1]. The following is a summary of the instruments used to acquire data.

2.2.1 Gas-concentration sensors

Three levels of gas-concentration sensors were installed at the 25 gas stations and 5 turbulence stations, for a total of 90 sensors. Thirty-three were infra-red sensors developed by LLNL, 45 were IST (International Sensor Technology) solid-state sensors, and 12 were MSA (Mine Safety Appliance) catalytic sensors. A prototype version of a JPL (Jet Propulsion Laboratory) infra-red sensor was fielded on Burros 7, 8 and 9, yielding data that agreed well with the LLNL infra-red sensor operating next to it.

2.2.1.1 LLNL infra-red sensors We developed the LLNL infra-red sensors because gas sensors suitable for use in LNG spills did not exist. What was needed was a fast, differential, infra-red absorption sensor that was portable, would work in the dense fog associated with LNG spills, and would detect separately methane, ethane and propane. The LLNL sensor [2] is fast and was developed to work in the fog (atmospheric water vapor condensed by cold LNG vapors) and to detect separately methane and ethane-plus-propane. The JPL sensor [3] is also fast, but was developed to work in fog-free regions and to detect separately methane, ethane and propane.

In the LLNL sensors, infra-red radiation from a source passes along an optical path open to the atmosphere. If hydrocarbons and/or water droplets are present, absorption (or scattering) occurs, and the amounts of absorption specific to methane, ethane-plus-propane, and fog are detected at a pyroelectric detector. Absorption specific to these species is defined by four narrow band-pass filters between 3.0 and 3.9 μm. In the absence of fog, the two middle bands are used to determine the methane and ethane-plus-propane concentrations, and the other two bands are used as reference channels to compensate for changes in system throughput resulting from dust on the lenses or temperature-induced baseline shifts. In the presence of fog, the two outer bands are also used to correct for spectral scattering due to fog particles. The calibration algorithms are based on experimental data for the hydrocarbons and on Mie scattering calculations and experimental data for fog obtained during the Burro 1 liquid-nitrogen spill. The single-gas calibration uncertainties were ±5.5% and ±2.5% of the gas-sensor reading, or ±0.9% and ±0.3% gas concentration for methane and ethane, respectively. Several calibration checks in the field have shown that the calibrations are quite stable in that they did not change over four months of operation in the desert environment. The overall accuracy of the system can be estimated by combining the gas-concentration results with a self-consistency examination of the data from Burro 1, which had fog but no hydrocarbon gas. For the great majority of the Burro 1 data, the results showed quite variable fog concentrations but essentially no apparent hydrocarbons. The dense fog caused some sharp spikes to occur in the methane and ethane-plus-propane channels. However, the apparent average methane and ethane-plus-propane concentrations during the time dense fog was present were only 0.1% and 0.9%, respectively. The overall uncertainty in either the methane or ethane-plus-propane results is about ±1% gas concentration in the presence of dense fog.

2.2.1.2 IST solid-state sensors The IST sensors were designed to detect hydrocarbon gas concentrations as high as 25%. They proved to be sensitive to humidity in the presence of methane, and they showed variable sensitivity to the higher hydrocarbons, ethane and propane. Corrections were developed for these effects and applied to the data. Some sensors exhibited calibration and gain changes during the course of the experiments; consequently, all sensors were recalibrated after completion of the effort at China Lake. The result of these corrections to the IST sensor data is a fairly high residual uncertainty in their accuracy. Our current estimate is that the uncertainty is 20—30% of the indicated value for concentrations less than 5% and, for higher concentrations, as high as 50% for some of the poorer sensors. When corrected IST data were compared with data from an LLNL infra-red sensor at the same location during Burros 8 and 9, they showed agreement to within about 10% of reading.

2.2.1.3 MSA catalytic sensors MSA sensors are well-understood, standard commercial units that operate on the catalytic principle and work well as long as the gas concentration remains below the stoichiometric mixture (10% for methane). The sensor response is very linear, and the uncertainty is about 10% of reading.

2.2.2 Humidity sensors

Eight humidity sensors were mounted at stations throughout the array, including one at upwind turbulence station T-1. These sensors were developed at LLNL specifically for use in cold fog. The sensitive element is the commercially available Humicap (Vaisala). The Humicap cannot tolerate contact with liquid water so it is protected by a porous sintered frit that is heated to 40°C to evaporate the water droplets. Calibration data indicate a linear response over the 10—60% relative humidity range at 40°C and a non-linear response below 10%. The average sensor calibration accuracy is ±0.5% relative humidity. Side-by-side comparisons of the instruments show agreement to better than ±2%, while long-term drift is estimated to be less than ±3% relative humidity.

2.2.3 Wind-field anemometers

The wind-field measurements were made by commercially available two-axis cup-and-vane anemometers (Met-One) located at 20 stations, 2 m above the ground, both upwind and downwind of the spill point. They have a starting threshold of 0.2 m/s and a response-distance constant of 1.5 m. Data taken by these instruments were averaged for 10 s before being transmitted to the data-recording trailer. The wind-field anemometers were calibrated with respect to three standards selected from the same batch. The standards were then sent to the National Bureau of Standards (NBS) for calibration in a wind tunnel, and the results of this calibration were used for final calibration of the field instruments. The uncertainty in speed for these instruments is ±1%, or 0.07 m/s.

2.2.4 Turbulence anemometers

The six turbulence stations used standard, commercially available bivane anemometers (R.M. Young Co.). Three of these anemometers were mounted on each tower at heights of 1.36, 3 and 8 m so that the vertical wind profile, as well as the various parameters related to atmospheric turbulence, could be determined. These anemometers have a starting threshold of 0.1—0.2 m/s and a response-distance constant of 1.0 m. Factory-supplied calibration curves were used, and data were taken at the rate of 3—5 Hz.

2.2.5 Heat-flux sensors

The heat-flux sensors were standard, commercially available heat-flux plates (Hy-Cal Engineering). They consisted of two layers of thermopiles separated by material of known thermal conductivity, forming a thin rectangular wafer that was buried just below the soil surface. These devices, along with the humidity sensors, were installed at seven downwind gas stations close to the array centerline.

2.2.6 Thermocouples

Standard Chromel-Alumel (type K) thermocouples were colocated with each gas sensor to provide temperature measurements of the gas cloud. The 10 mil thermocouples had a response time of about 0.5 s in a 5 m/s wind, corresponding roughly with the infra-red gas sensors on the gas stations, which averaged data for 1 s. Data from the upwind NWC meteorological tower were used to determine the atmospheric temperature gradient in the lower 15 m.

2.2.7 Cameras

Photography was an important diagnostic tool, and cameras were in operation in all experiments except Burro 7. Remotely controlled 16 mm motion picture cameras were used in three locations. The crosswind camera was on top of the control bunker, about 220 m from the spill point. The upwind camera was about 70 m upwind of the spill point (close to T-1) and about 1.5 m above ground level. The overhead camera was about 120 m north (downwind) of the spill point and about 45 m above ground level. The cameras were supplied by NWC personnel and operated from the bunker.

2.2.8 Infra-red imagers

The EG & G Remote Measurements group provided infra-red imaging of several spills (Burros 2, 4, 6 and 9), using a helicopter-mounted Inframetrics dual-band infra-red imager. The instrument had two channels — one sensitive to radiation with wavelengths between 4 and 6.5 μm and one sensitive to radiation with wavelengths between 7 and 14 μm. A strong methane infra-red absorption band between 7 and 8.5 μm should allow the methane cloud to be imaged in the long-wavelength channel, using the ground as a thermal radiation source.

The overflights were successful in imaging the gas cloud as it dispersed downwind. Traces of the cloud were seen, in the 7—14 μm channel, as far downwind as 1500 m, where the gas concentration would have been substantially less than 1%. Unfortunately, the cold gas also cooled the ground, changing the source characteristics. Consequently, the observed image was a combination of methane absorption and the cold-ground effect. These two effects will be separated in future work. An attempt was made to measure the size of the LNG pool on the Burro 9 experiment by reducing the imager sensitivity to see through the dense fog and image the LNG pool against the water.

2.3 Data recording and storage

Data were transmitted from the stations to a central data-recording trailer, where they were written onto a disk. After each experiment, the data were written onto magnetic tape and shipped back to Livermore, where they were transferred to the MASS storage system [4] at the LLNL Computation Center for archival preservation. Most data manipulation, plotting, and contour generation were done with data-base files, created by the data-base management system FRAMIS [5], using an LLNL-developed data-analysis system called MATHSY [6]. This interactive, array-processing, mathematics and graphics system has been a powerful tool for analyzing, handling and displaying the large quantities of data from the Burro experiments.

2.4 Test summary

Table 1 is a summary of the test and meteorological conditions for the eight LNG spills in the Burro series. Using wind-field data from the twenty 2-m-high anemometer stations, the mean and standard deviations for wind direction and wind speed were calculated over a 6 min period that began at the start of the spill. The descriptive atmospheric-stability category is based on the Richardson number. The numerical values for atmospheric-stability indices and other meteorological parameters were determined as described in [1] and as summarized below.

The temperature and temperature-difference values used to calculate T_* were measured on an upwind NWC meteorological tower close to turbulence tower T-1. Temperature was measured at a height of 2 m, and temperature difference was measured between the 2 m sensor and sensors at heights of 1, 5, 10 and 15 m.

The T_* values did not vary significantly during any experiment. The friction velocity, u star (u_*), was diabatically adjusted (i.e. corrected for non-adiabatic effects of atmospheric stability) and was derived from turbulence-tower and wind-field data, and the corresponding roughness length (z_0) was approximately constant at $z_0 = 2.05 \times 10^{-4}$ m for all experiments.

The interrelated parameters (Richardson number, R; Monin-Obukhov length, L; turbulent Prandtl number, α; sensible heat flux, H; and diabatically adjusted momentum diffusivity, K) were calculated from the temperature

TABLE 1

Burro experiment summary and ambient meteorological parameters (see symbols)

Parameter	Experiment							
	Burro 2	Burro 3	Burro 4	Burro 5	Burro 6	Burro 7	Burro 8	Burro 9
Date	6/18/80	7/2/80	7/9/80	7/16/80	8/5/80	8/27/80	9/3/80	9/17/80
Q (m^3)	34.3	34.0	35.3	35.8	27.5	39.4	28.4	24.2
dQ/dt (m^3/min)	11.9	12.2	12.1	11.3	12.8	13.6	16.0	18.4
u (m/s)	5.4 ± 1.8	5.4 ± 1.2	9.0 ± 1.2	7.4 ± 1.1	9.1 ± 1.1	8.4 ± 1.2	1.8 ± 0.3	5.7 ± 0.7
θ (deg)	221 ± 14	224 ± 13	217 ± 7	218 ± 11	220 ± 7	208 ± 5	235 ± 6	232 ± 4
Wind-speed tendency	Decreasing	Fairly constant	Fairly constant	Fairly constant	Fairly constant	Nearly constant	Decreasing	Slowly decreasing
Atmospheric stability	Unstable	Unstable	Slightly unstable	Slightly unstable	Slightly unstable	Neutral to slightly unstable	Slightly stable	Neutral
Humidity (%)	7	5	2	6	5	7	5	12
T_2 (°C)	37.6	33.8	35.3	40.5	39.2	33.7	33.1	35.4
T_* (°C)	−0.57	−0.65	−0.65	−0.60	−0.57	−0.23	+0.145	−0.100
u_* (m/s)	0.248	0.249	0.403	0.333	0.406	0.372	0.074	0.252
α	1.40	1.46	1.17	1.23	1.14	1.06	0.623	1.05
H (W/m^2)	−122	−154	−159	−131	−132	−41	+2.2	−10
K_m (m^2/s)	0.278	0.291	0.377	0.327	0.371	0.316	0.037	0.212
R_2	−0.178	−0.221	−0.054	−0.079	−0.044	−0.018	+0.121	−0.014
L (m)	−11.2	−9.06	−37.1	−25.5	−45.8	−114	+16.5	−140

Symbols

- Q = spill volume.
- dQ/dt = spill rate.
- u = mean and standard deviation of wind speed at 2 m height.
- θ = mean and standard deviation of wind direction.
- T_2 = temperature at 2 m height.
- T_* = $dT/d \ln z$.
- u_* = friction velocity, diabatically adjusted.
- α = turbulent Prandtl number, K_h/K_m
- H = sensible heat flux, negative upward.
- K_m = momentum diffusivity at 2 m height.
- R_2 = Richardson number at 2 m height.
- L = Monin—Obukhov length scale.
- K_h = heat diffusivity at 2 m height.

and wind-velocity profiles in accordance with the theory of Dyer and Businer [7,8], as modified by Lettau [9].

3. Vapor dispersion

3.1 General analysis

3.1.1 Pool size

The airborne infra-red imager was used to measure pool size during the Burro 9 experiment. Its sensitivity was reduced in an attempt to see through the fog and image the LNG pool against the warm pond. The observed image was about 10 m in diameter; however, this should not be considered representative of other experiments since RPT's blew away the spill plate early in the test, drastically changing the nature of the LNG pool on the water surface.

3.1.2 Gas-concentration contours

The LNG vapor-concentration data were used to generate two-dimensional contour plots at 10 s time intervals during the experiments. A 10 s average was chosen somewhat arbitrarily; the intent was to use an averaging time that was long enough to average out short-wavelength (much less than cloud width) fluctuations, but short enough to preserve cloud meander. Contour plots are generated for several surfaces; horizontal surfaces at heights of 1 and 3 m above the ground, and vertical crosswind cylindrical surfaces at each row of the sensor array. The contours are of total hydrocarbon concentration, with the data from the LLNL infra-red methane and ethane-plus-propane channels being combined to correspond to the IST and MSA total hydrocarbon measurements. Data from the faster response-time instruments are also averaged, using a 10 s running average, so that all the data have approximately the same time constant. Therefore, the contours describe the 10-s-average LNG vapor-concentration distribution on a surface at a given time.

The horizontal contours are calculated over a region that extends downwind from the spill point ($x = 0$) to the final row of sensors at 800 m (see Fig. 2). To close the contours in the source region, the concentration at $x = 0$ is arbitrarily defined by a hyperbolic concentration distribution that is held constant during the spill and that is decreased linearly to zero after the spill valve is closed.

In both the horizontal and vertical contour-plot concentrations, a "dummy" station is added to both ends of each sensor row at a distance equal to the station spacing for that row. When the LNG vapor cloud is well within the array and the concentration at the end of the row is essentially zero (<1%), the concentration at the corresponding "dummy" sensor is set equal to zero. If part of the cloud extends beyond the edge of the array, the "dummy" sensors are ignored and the contours are truncated at the edge of the array.

The gas concentration at each station location is set equal to zero at a height of 12 m. The concentration at the ground is extrapolated from the measured values at heights of 1 and 3 m. When the 3 m concentration is less than the 1 m value, the ground-level concentration is determined by using a quadratic extrapolation that passes through the 1 and 3 m concentration values and has a zero concentration gradient at the ground. For those cases where the 3 m concentration is greater than the 1 m value, the ground-level concentration is linearly extrapolated from these two values. Concentrations at points within the calculational region are determined by a linear interpolation in three dimensions.

Interpolating over the long distances between sensors in the 140, 400 and 800 m arcs produces some uncertainty in the calculation of gas-concentration values between these arcs. A linear interpolation scheme was used because of its inherent simplicity and ease of interpretation. If different interpolation schemes are used, different results will be obtained between arcs. In particular, the distance to the lower flammability limit (LFL), i.e., the 5% contour for methane, is generally between the 140 and 400 m arcs for these tests. If we use Burro 3 as an example, the linear interpolation scheme produces an LFL distance of 255 m maximum. If the concentration is assumed to decrease with downwind distance as x^{-n}, then LFL distances of 252, 207 and 188 m are obtained for n = 1.0, 1.5 and 2.0, respectively. Thus it appears that linear interpolation gives a maximum LFL distance. Analysis of contours from all of the experiments indicates that the uncertainty in the LFL distance is approximately –40 to +20 m.

Since the distances between sensors on a tower and stations in an arc are much less than the distances between arcs, the uncertainty in contour location is much less for the vertical contours than it is for the horizontal contours. We estimate the uncertainty in the position of the vertical contours to be less than 1 m.

3.1.3 Cloud-centerline calculations

The cloud-centerline calculation is performed with the ATMAS atmospheric transport code [10]. Using wind-velocity data obtained from the 20 wind-field stations and applying a $1/r$ interpolation-extrapolation scheme, the code estimates the wind velocity over the entire region of interest. Every 10 s the wind field is updated with new 10-s-averaged wind-velocity data. The cloud centerline is generated by creating, every 2.5 s, a marker particle (conceptionally, using ATMAS) at the spill point and then allowing it to be transported by the wind field. ATMAS calculates the marker-particle trajectories, using the atmospheric advection-diffusion equation with the diffusion terms set equal to zero. The positions of the marker particles constitute the cloud centerline.

In general, the agreement between the wind-field calculated cloud centerline and the orientation of the horizontal gas-concentration contours is quite good. This is especially true when the centerline is near the center of

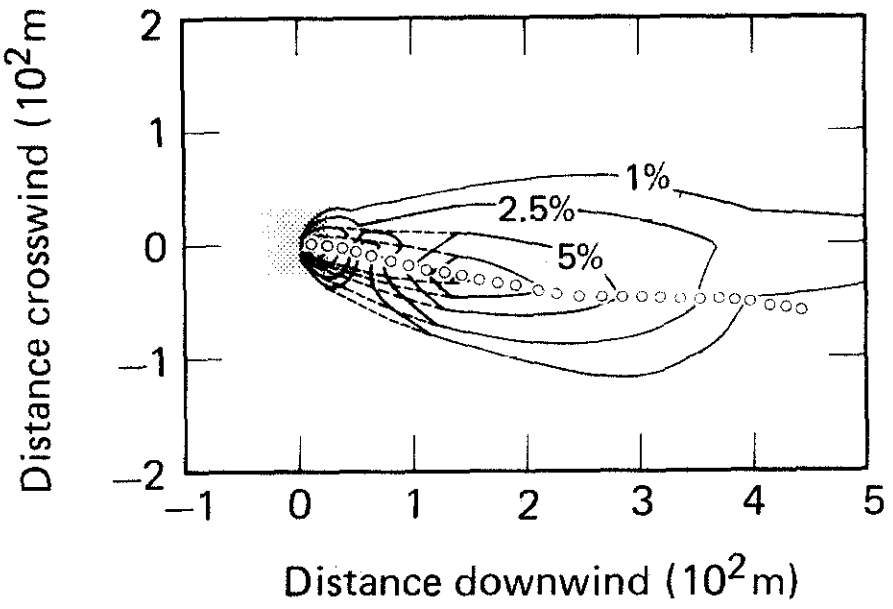

Fig. 5. Horizontal gas-concentration contours and central wind-field flowline for the Burro 9 experiment. Contours shown are 1, 2.5, 5, 7.5 and 10% by volume.

the array, as was the case with Burro 9, as shown in Fig. 5. Although there were a few exceptions to this good agreement, they usually resulted from the presence of inoperative gas sensors, which tended to distort the concentration contours. The agreement was also somewhat poorer near the edges of the array, as in the Burro 7 experiment, primarily because of the lack of wind-velocity data in the regions near the edges of the array and because of the $1/r$ interpolation-extrapolation scheme used in ATMAS being somewhat biased in these regions.

3.1.4 Mass-flux calculations

The calculation of the mass flux of gas through an arc of gas-sensor stations can be used to determine indirectly the vapor generation rate on the spill pond. This is important since vapor generation was not measured directly. If the mass flux is integrated over time, it can be compared with the total quantity of LNG spilled to determine the mass balance and how well the array was able to measure the dispersing gas cloud. Such an evaluation is necessary to determine whether the number of sensors and their locations provided adequate coverage. Mass flux was calculated for the 140 m arc for Burros 8 and 9. Because of the low wind conditions for Burro 8, the cloud spread exceeded the width of the array, but most of the cloud was measured. On Burro 9, the entire cloud remained within the array as it traveled downwind; consequently, it provides a good test of mass balance.

The spatially integrated mass flux $F(t)$ through the cylindrical surface of radius r, centered on the spill point at time t, is given by

$$F(t) = \frac{pM}{R} \int_z \int_\theta \frac{c(z,\theta,t)u(z,\theta,t)}{T(z,\theta,t)} r\,d\theta\,dz \qquad (1)$$

where p is ambient atmospheric pressure, M is molecular weight, R is the

gas constant, c is gas concentration, u is the wind component normal to arc, T is temperature, θ is direction and z is height. The cumulative mass is obtained by integrating eqn. (1) over time. Equation (1) is integrated numerically, with accuracy being dependent on the number of points used to approximate the integrand in space and time.

Gas-concentration values were interpolated by appropriate linear and quadratic relations described in the previous section. Wind-speed interpolation was logarithmic with height, and temperature interpolation was logarithmic with height from 0.1—1 m and linear above that.

Results of the mass-flux calculations for Burro 9 are presented in Fig. 6a. Integrating the interpolated data gives an integrated mass flux, shown by the dotted line. The arrival and departure of the cloud are quite obvious.

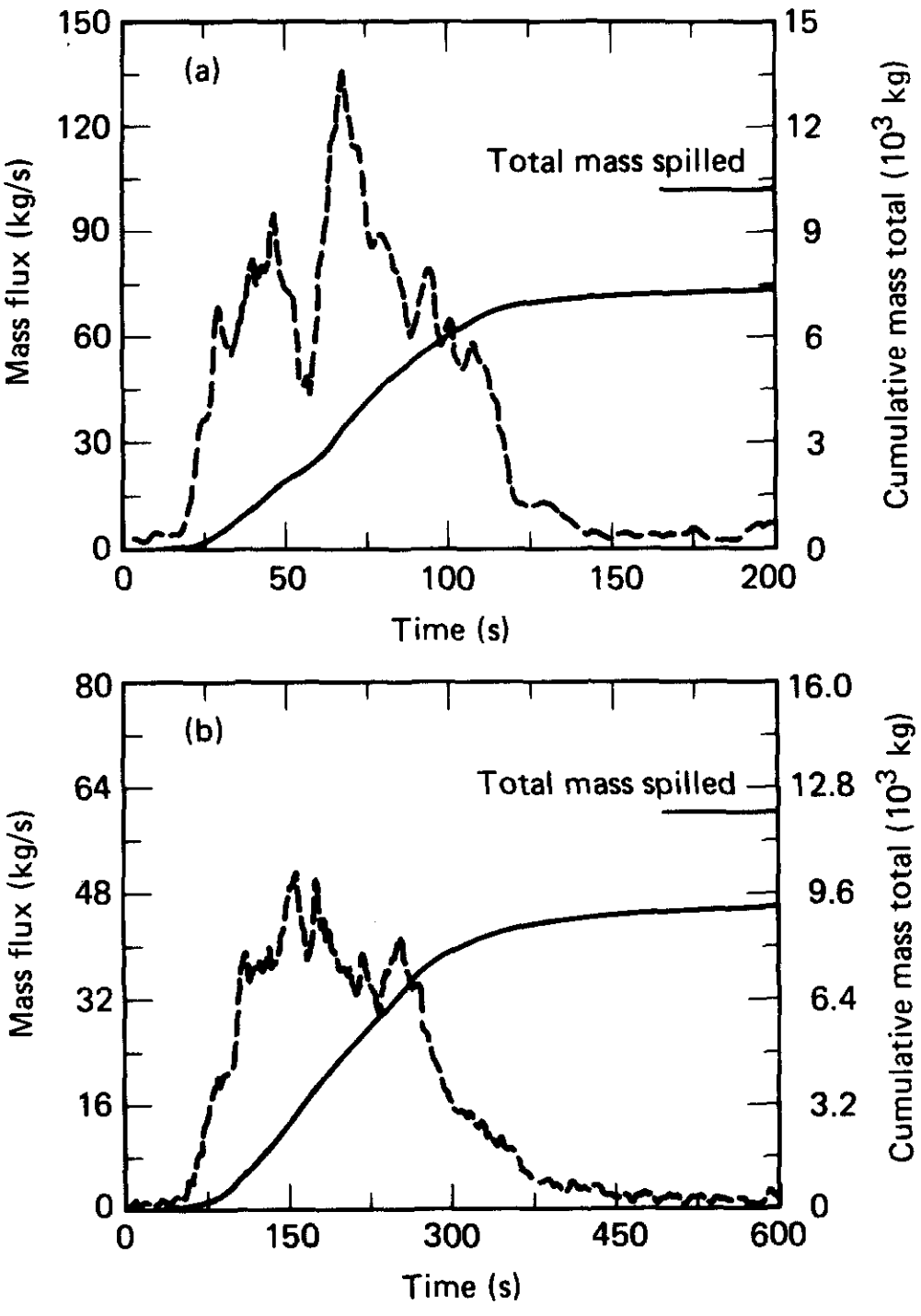

Fig. 6. Mass flux and integrated total mass (a) Burro 9 and (b) Burro 8 (140 m arc).

The decrease in flux between 45 and 70 s is attributed to RPT's disrupting the vapor source. After integrating the flux from 0—200 s, a total mass of 7439 kg is calculated to have passed through the 140 m arc. This represents 72.3% of the 10285 kg spilled, and is a reasonably good accounting of the mass released. Errors in the gas-sensor calibrations would contribute to this discrepancy, as would the generally sparse nature of the gas-sampling (particularly in the vertical) array. The major source of uncertainty is probably due to the mud and water thrown on the sensors by the large RPT's. The readings appear to have been lowered enough on at least one of the stations to account for most of the 28% of the gas missing from the analysis. Taking this into account, the degree of agreement is quite satisfactory and indicates a good overall accounting of the gas-cloud and sensor calibrations.

Burro 8 was not affected by RPT's. Results of the mass-flux calculations are presented in Fig. 6b. The mass flux shows the arrival and rather gradual departure of the cloud. Integrating from 0—600 s gives a total measured mass of 9193 kg through the 140 m arc, or 76.2% of the total spilled (12,070 kg). Overhead photography indicated that the cloud spread was greater than the width of the array, an observation supported by significant measured gas concentrations at both edges of the array. It appears that most of the cloud was contained within the 140 m arc and that concentrations beyond the edge towers probably dropped off quite rapidly.

3.2 Gas-cloud characteristics

As defined by the data in Table 1, the Burro experiments may be grouped into four categories according to the conditions for the experiments: (1) Burros 2 and 3 for low spill rates, moderate wind speeds, and unstable atmospheric conditions; (2) Burros 4—7 for low spill rates, high wind speeds, and unstable atmospheric conditions; (3) Burro 8 for high spill rate, very low wind speed, and slightly stable conditions; and (4) Burro 9 for high spill rate, moderate wind speed, and neutral atmospheric stability.

The gas-cloud centerline was best aligned with the array centerline for Burros 3, 5, 8 and 9. The array of operational gas sensors (see Fig. 2) was most complete for Burros 7-9, but RPT's adversely affected the sensors in the 57 m arc during Burros 6 and 9.

After considering the above, Burros 3, 7, 8 and 9 were selected for discussion of gas-cloud characteristics, one from each experimental category.

3.2.1 Burro 3

The Burro 3 cloud remained within the array, except at the 57 m arc, where it extended beyond both sides of the array between 150 and 200 s. The downwind location of the lower flammable limit (LFL), corresponding to 5% volumetric gas concentration at the 1 m level, is plotted for Burro 3 as a function of time in Fig. 7, together with similar plots for the other selected experiments. The downwind tip of the region enclosed by the 5% contour (LFL contour) extended to a maximum downwind distance of

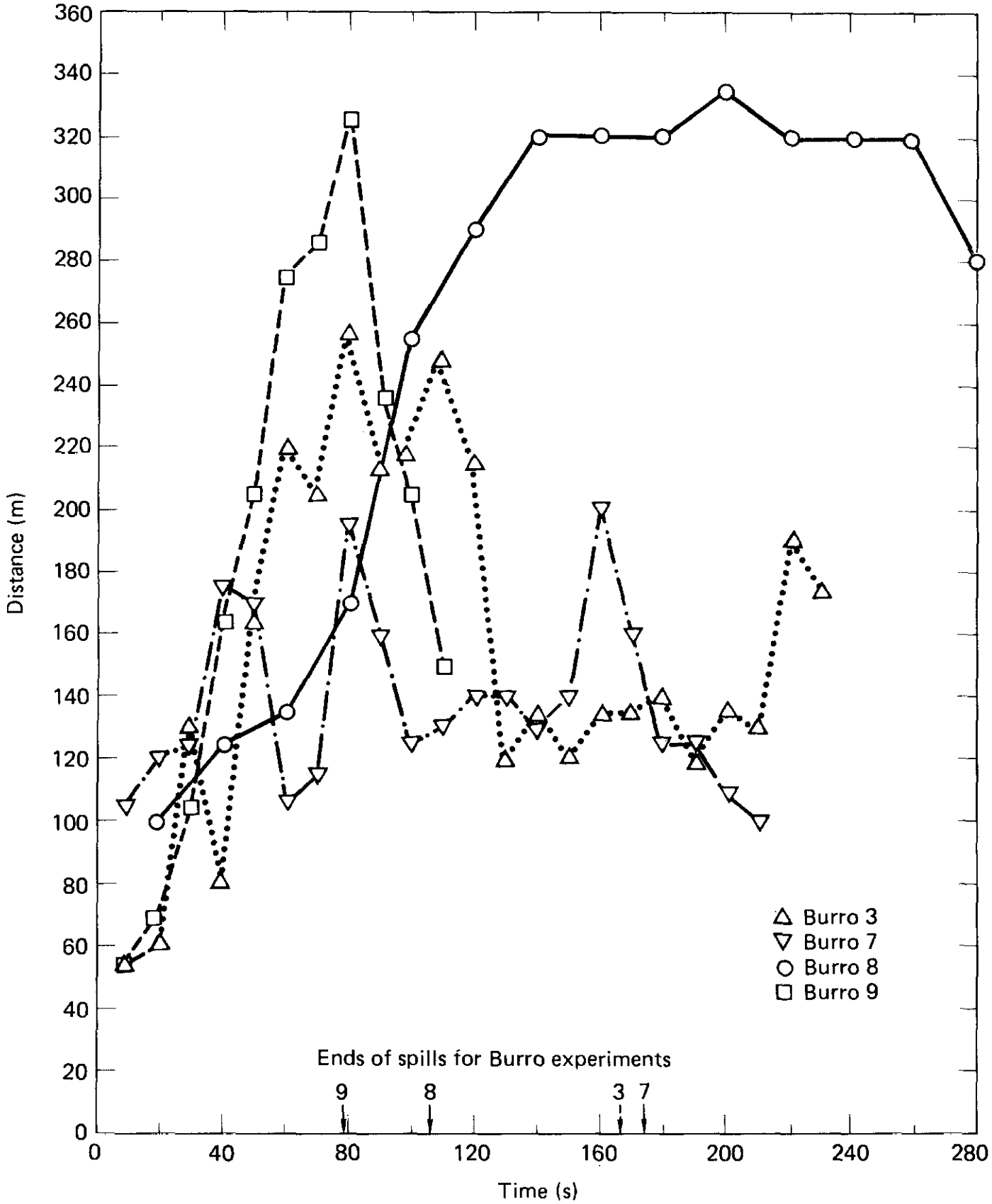

Fig. 7. Radial downwind distance to lower flammable limit (LFL) from gas-concentration contours at 1-m elevation for Burros 3, 7, 8 and 9.

270 m, with a width of about 80 m between 60 and 120 s (see Fig. 8). At about 150 s, the distance to the LFL decreased to about 100 m and the cloud bifurcated, producing high concentrations at the outer stations in the 57 m arc. Cloud bifurcation occurred during several experiments, and it appears to have been caused mainly by aerodynamic interaction between the gas cloud and the wind. The bifurcation disappeared at 190 s and the LFL

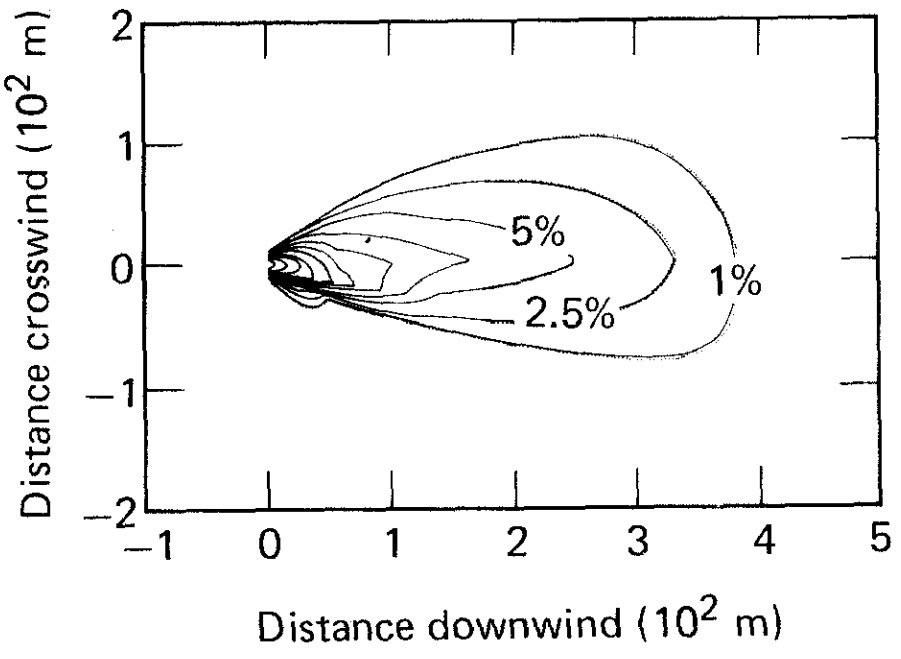

Fig. 8. Horizontal concentration contours for Burro 3, showing cloud shape during maximum downwind extent of the LFL. Gas-concentration contours are 1, 2.5, 7.5, 10, 12.5 and 15% by volume.

moved downwind again at 220 s, after shutdown but before the cloud dissipated. The downwind extent of the cloud for any value of gas concentration was always less at the 3 m level than it was at the 1 m level, and the gas concentration decreased with height at all instrument arcs. The downwind location of the upper flammable limit (UFL), corresponding to 15% volumetric gas concentration, was almost always upwind of the 57 m arc, except during cloud bifurcation at 50 s and again at 150—180 s, when it extended to about 70 m downwind.

3.2.2 Burro 7

The Burro 7 cloud always extended beyond one edge of the array, but the cloud centerline appeared to move on and off the array several times during the spill. Burro 7 is an excellent example of cloud meander. The downwind location of the LFL for Burro 7, at the 1 m level, is plotted as a function of time in Fig. 7. The LFL location oscillated between about 100 and 200 m. Most of this variation was caused by the meandering of the cloud relative to the edge of the array (see Figs. 9, 10a and 10b), but some may have been caused by bifurcation of the 5% contour. The vertical gas-concentration contours for the 57, 140 and 400 m arcs showed less and less of the cloud within the array with increasing downwind distance. Because of this trend and the cloud meander, the location of the LFL is uncertain. Gas concentration decreased with height at all instrument arcs. The downwind location of the UFL was slightly downwind of the 57 m row (perhaps 20 m) during much of the spill, but the true location is uncertain because these high concentrations occurred at the end of the 57 m arc.

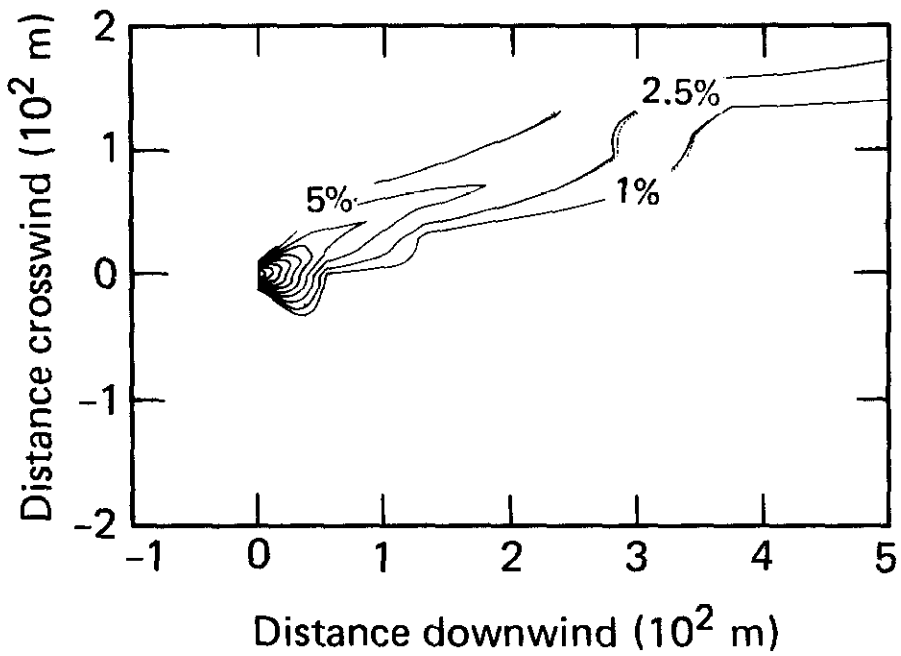

Fig. 9. Horizontal concentration contours for Burro 7, showing typical alignment along the edge of the array. Gas-concentration contours are 1, 2.5, 5, 7.5, 10, 12.5 and 15% by volume.

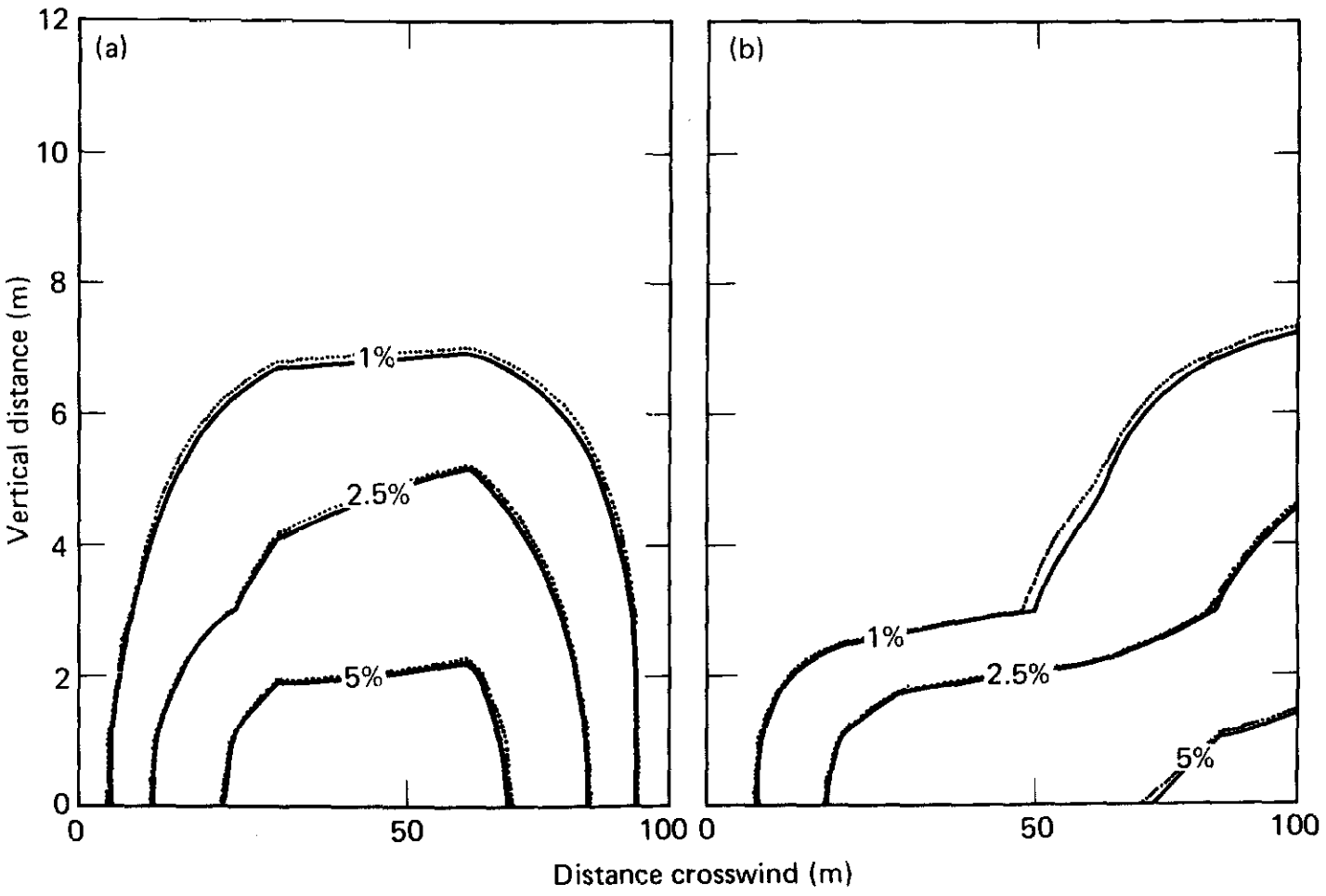

Fig. 10. Vertical concentration contours, 140 m arc, showing Burro 7 cloud meander (a) within array at 160 s and (b) over edge of array at 170 s.

3.2.3 Burro 8

The Burro 8 cloud was centered, but extended beyond both sides of the array. However, mass-balance calculations indicate that most of the gas was accounted for within the array. The downwind location of the LFL for Burro 8, at the 1 m level, is plotted as a function of time in Fig. 7. Only in this case did the LFL appear to stabilize at a given location, approximately 320 m. However, concentrations above 5% were detected at the 3 m level at the end of the 400 m row late in the spill.

The Burro 8 cloud is especially interesting because the very low wind speed permitted the gravity flow of the cold, dense gas to be almost independent of the surrounding atmospheric boundary layer. Photography showed that the cloud extended about 40 m upwind of the spill point, as well as beyond both sides of the array. Figure 11 is an overhead photograph of the Burro 8 cloud during the spill. The facility can be seen at the far right, and the towers in the 57 m arc can be seen in the middle of the cloud. The cloud was wider and lower in height than that from any of the other Burro experiments. Figure 12a shows the 1 m gas-concentration contours at 200 s; this example is representative of these contours from about 100—260 s. As shown the cloud was bifurcated much of the time, probably because of the interaction between the lateral gravity flow and the longitudinal atmospheric flow. The cloud, therefore, tended to divide into two lobes that also appeared to be affected by the terrain. The flow of the up-

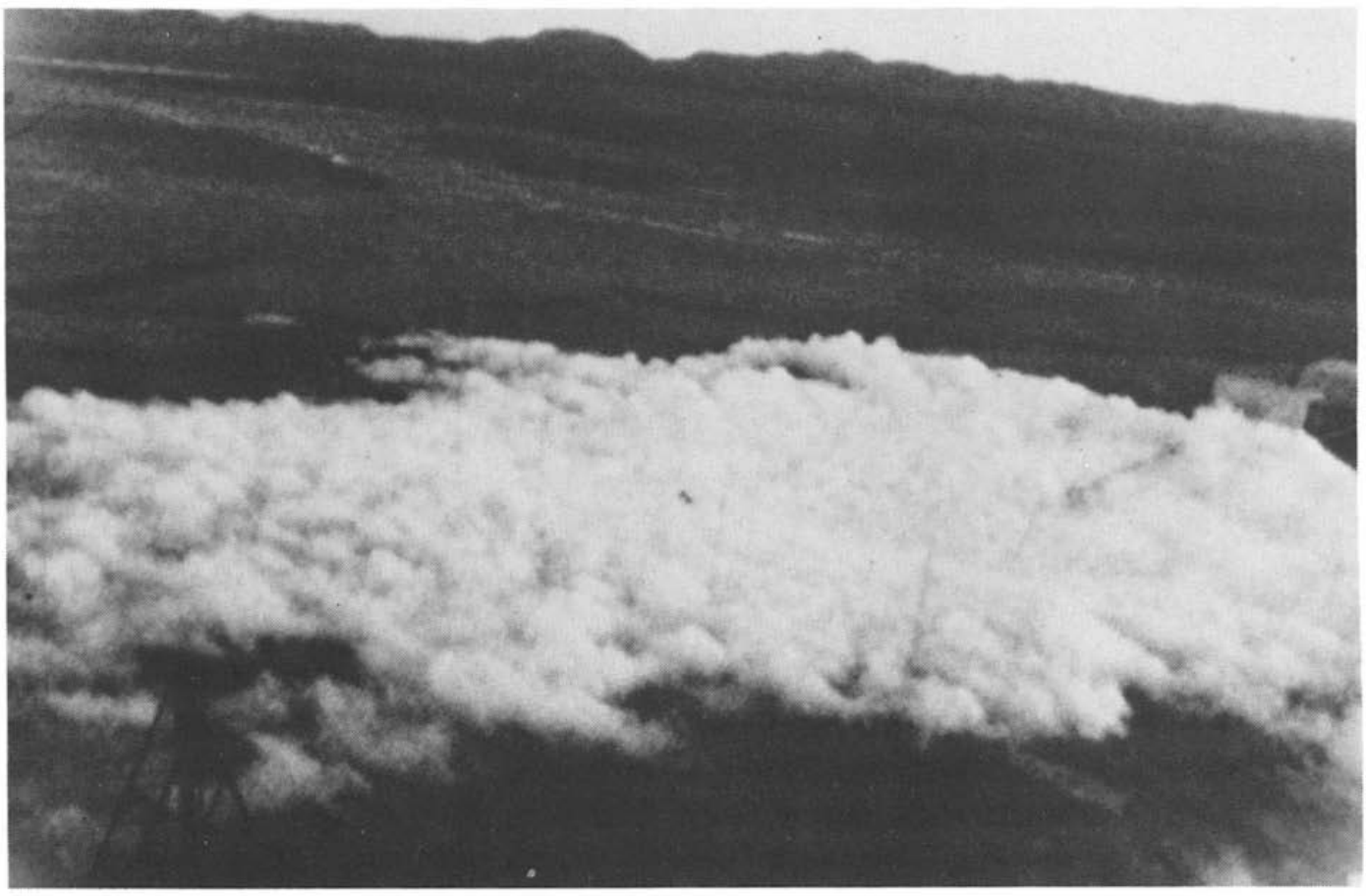

Fig. 11. Overhead view of the Burro 8 cloud. The spill facility can be seen at far right, with the spill pipe extending out into the cloud. Towers from the 57 m arc can be seen in the center of the cloud.

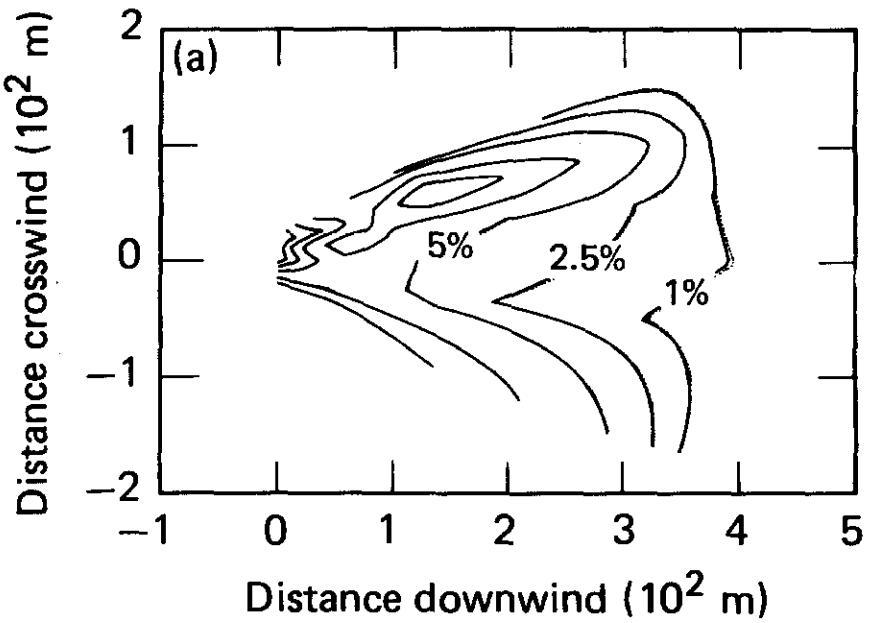

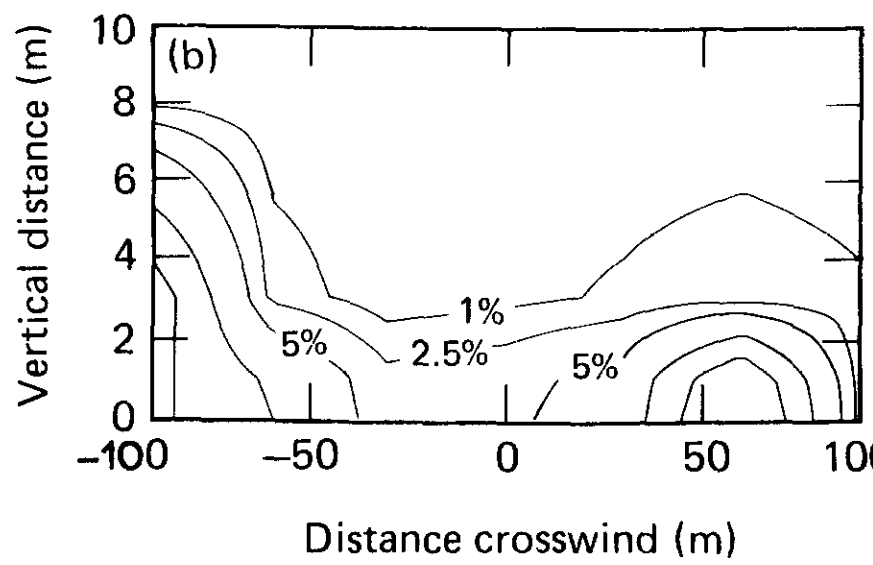

Fig. 12. Gas-concentration contours, showing Burro 8 bifurcated cloud configuration (a) horizontally at 1 m elevation and (b) vertically at 140 m arc at 200 s. Contours are plotted as though the reader were looking back toward the spill pond and are shown for 1, 2.5, 5, 10, 15 and 25% by volume in each case.

per one in Fig. 12a is uphill (see Fig. 2), and the lower one is along the edge of the dry lake bed. Consequently, there is probably more gas in the lower (left) lobe than in the upper (right) lobe, as shown in Fig. 12b. The cloud height measured at the 57 m arc was much less than that for the other experiments. For example, the sensors at the 3 m elevation in the 57 m arc did not detect any gas until between 100 and 120 s, even though many of the sensors at 1 m detected gas at 20 s. The LFL at the 1 m level extended about the same distance downwind in both lobes (about 320 m, see Figs. 6 and 12a). However, the maximum concentration in the lower lobe (left in Fig. 12b) may have been missed since ~5% concentrations were detected at the left edge of the 400 m row, at the 3 m level, between 400 and 500 s, which may have been due to the meander of this part of the cloud back across the sensors.

3.2.4 Burro 9

The cloud was within the array for the entire test, and most of the gas sensors were operational on Burro 9. Unfortunately, RPT explosions adversely affected the data from the 57 m arc and slightly affected data from the 140 m arc. The downwind location of the LFL for Burro 9, at the 1 m level, is plotted as a function of time in Fig. 7. The LFL location did not stabilize during the short spill (only 79 s); the 1 m contour plot in Fig. 13 shows its maximum extent to 350 m, with a width of about 75 m, at 80 s.

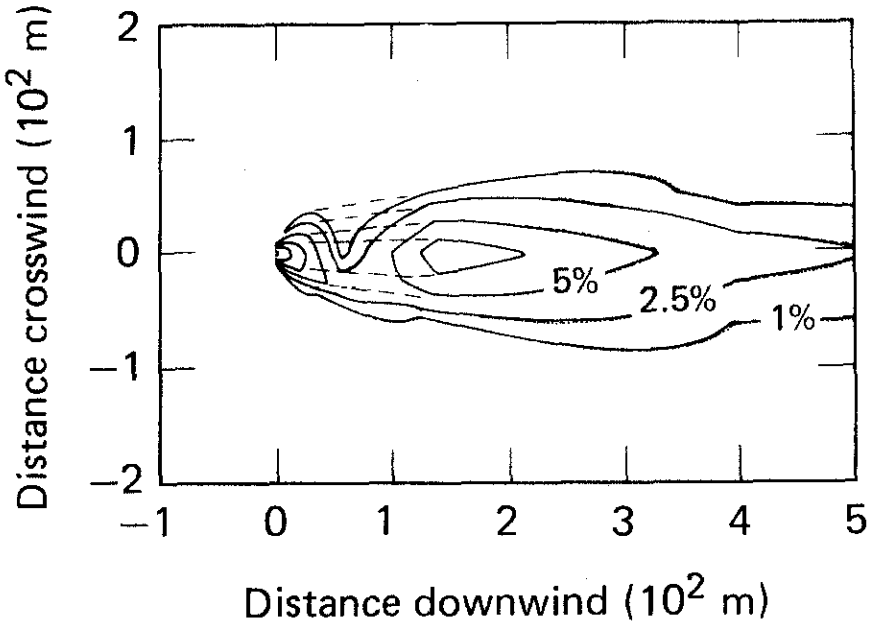

Fig. 13. Horizontal concentration contours for Burro 9 at 80 s, showing maximum downwind extent of the LFL. The dotted lines represent an attempt to correct for the effect of the RPT explosions on the sensors. Gas-concentration contours are shown for 1, 2.5, 5, 7.5 and 10% by volume.

The constriction in the contours at the 57 m row is a consequence of the effects of the RPT explosions on those gas sensors; the dotted lines represent our estimate of the actual contours. The high-concentration core of the gas cloud "lifted off" the surface between 140 and 400 m, as shown in Figs. 14a and 14b. This is believed to be a result of atmospheric boundary layer shear stress, not buoyancy [11]. It is not possible to make a statement about the UFL location because of the effects of the RPT explosions on the gas sensors in the 57 m row.

3.3 Gas-concentration statistics

As noted above, data were taken at a rate of 3—5 Hz at the turbulence stations and were smoothed before being used with data from other stations to generate the gas-concentration contours that represent 10-s-average concentrations. The methane channels of the LLNL infra-red sensors were relatively noise-free down to 10 s mean-concentrations of a few tenths of a percent. To better understand the significance of fluctuations about the 10-s-average values, unsmoothed 3—5 Hz data from the methane channels of the

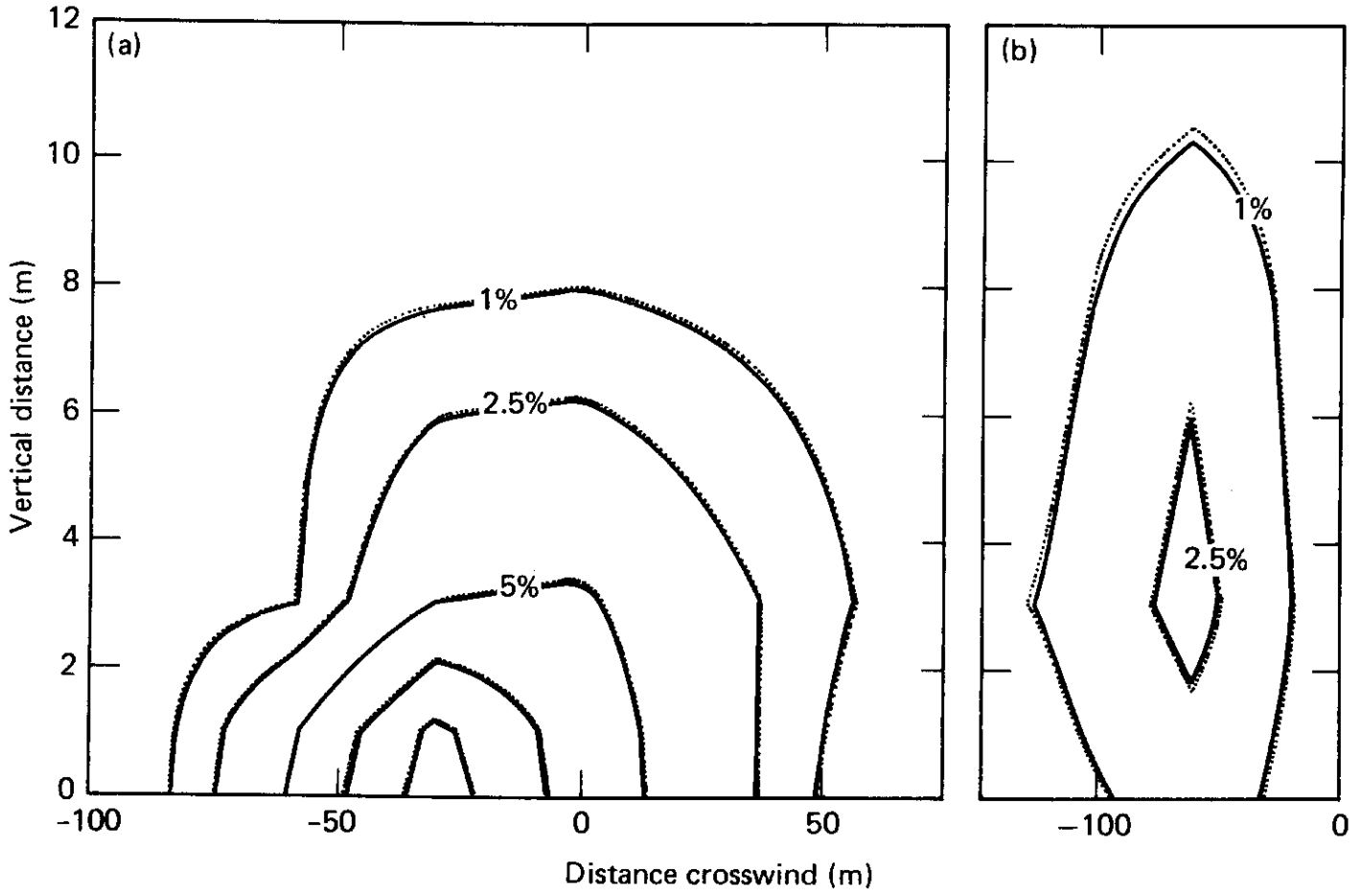

Fig. 14. Vertical concentration contours for Burro 9, showing cloud liftoff, with highest concentration (a) on surface at 140 m arc and (b) above surface at 400 m arc. Contours are shown for 1, 2.5, 5, 7.5 and 10% by volume.

turbulence station sensors were processed to obtain peak concentration values and standard deviations from the mean for Burros 7, 8 and 9.

A total of 555 ten-second samples were obtained from mean concentrations of 0.1% and greater; 50 for Burro 7, 414 for Burro 8, and 91 for Burro 9. The peak-to-mean methane concentration ratios for these 555 samples are plotted vs. methane concentration in Fig. 15. Note the general trend for increasing peak-to-mean concentration ratio with decreasing mean concentration. Almost all peak-to-mean ratios greater than two to three are associated with one or more zero values of gas concentration in the 10 s sample. Note also that, at mean concentrations of 0.5% and greater, peak-to-mean ratios higher than three are not very likely. Attention is called to two limit lines of peak-to-mean ratio vs. mean concentration: one for 15% peak volumetric concentration (the upper flammability limit), the other for 5% volumetric concentration (the LFL for methane). Points on or between these lines are associated with gas concentrations in the flammable range. Thus, we see that flammable peak concentrations of 5% or more are not uncommon for mean concentrations above 1%.

Concentration fluctuations about the LFL (5% for methane) are of special interest. A total of 100 10-s samples were obtained for mean concentrations ranging from 2.5—10%: 25 for Burro 7, 58 for Burro 8, and 17 for Burro 9. The ratios of the peak-minus-mean to the standard devia-

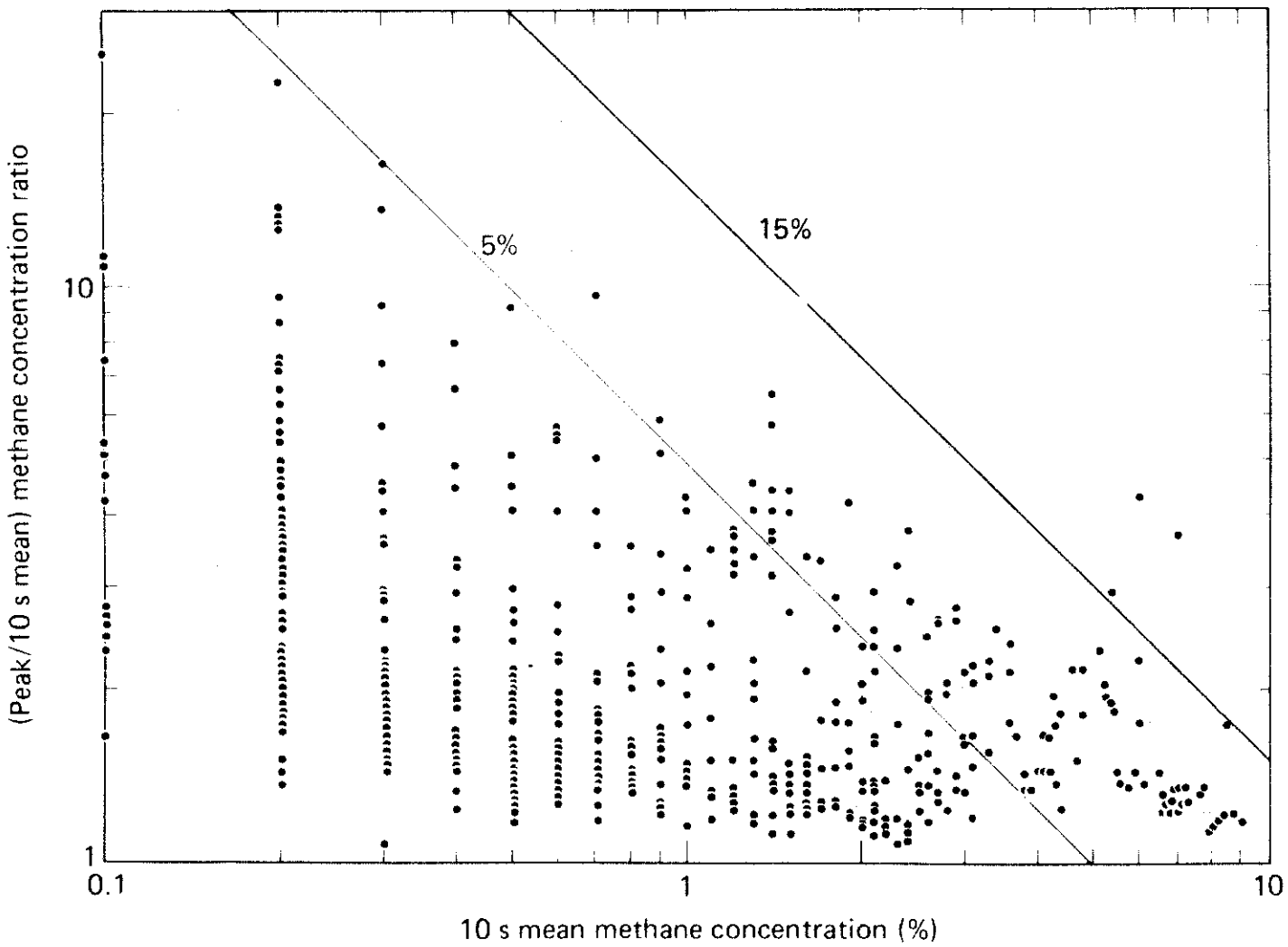

Fig. 15. Peak-to-mean concentration ratio vs. mean concentration for Burros 7, 8 and 9. Points between the diagonal lines are within the flammable limits.

tions from the mean were calculated for these 100 points. Assuming a log-normal distribution for these fluctuations and their ratio [11], the following geometric mean values were determined for the ratio of the peak-minus-mean to the standard deviation from the mean: 2.54 for Burro 7, 1.78 for Burro 8, and 2.18 for Burro 9. These values of approximately 2 are consistent with the lower range of values for peak-to-mean vs. logarithmic standard deviation presented in [11].

4. Gas-cloud dynamics and thermodynamics

4.1 Momentum displacement by cold gas

In most experiments, the horizontal wind field was not obviously affected by the presence of the cold gas cloud. However on Burro 8, with the lowest wind speeds (see Table 1), the mean flow was observed to diverge around the cold cloud and was reduced significantly within the cloud, as shown in Fig. 16. The mean wind speed, u (based on a 60 s averaging window), at 1.36, 3 and 8 m during Burro 8 is plotted in Fig. 16a for station T-1 (upwind) and in Fig. 16b for station T-2 (downwind). It is clear that the introduction of the cold gas cloud significantly perturbed the wind

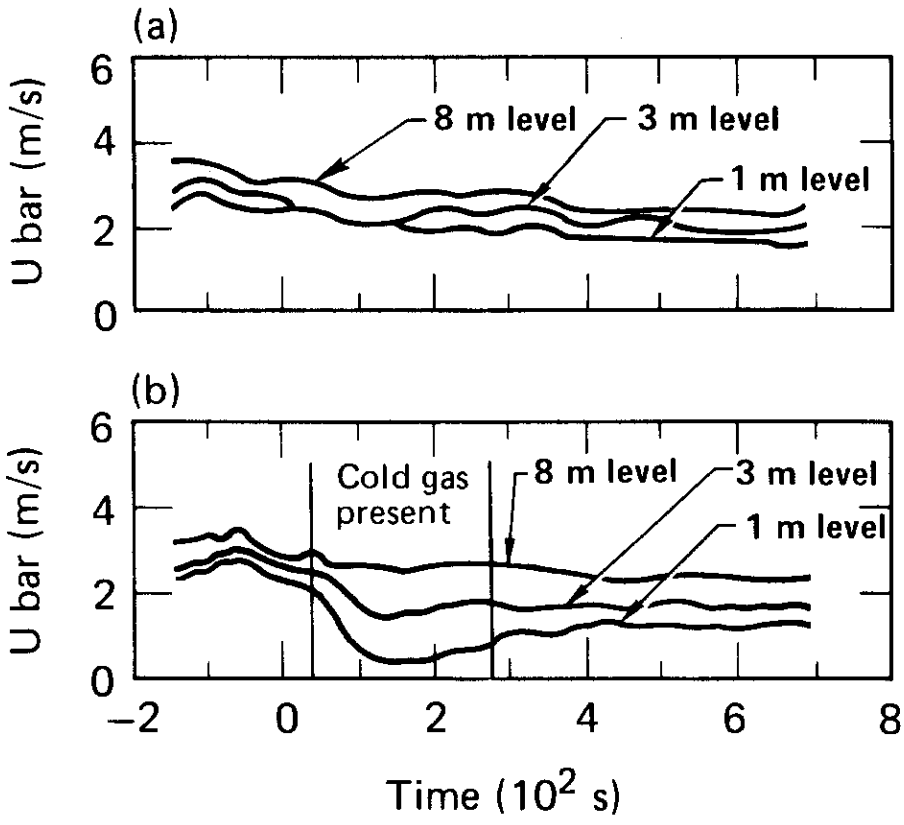

Fig. 16. Mean wind speed during Burro 8, (a) at station T-1 upwind of the spill pond and (b) at station T-2 downwind of the spill pond and within the gas cloud.

field near the ground. Similar mean wind-speed plots for Burro 7 and Burro 9 did not show such an effect.

To quantify the effect of the cold gas on the flow field, we used profiles of mean wind speed at stations T-1 and T-2 to estimate displacement thickness — a measure of how boundary layer flow tends to be displaced upward by the introduction of cold gas. The displacement thickness δ is obtained by vertically integrating the momentum defect profile, F,

$$\delta(t) = \int_z F(t)\,dz \approx \sum_{i=1}^{n} F_i \Delta z_i \tag{2}$$

The momentum defect profile, as defined here, is a relative measure of the momentum loss downwind of a thermal discontinuity, expressed for stations T-1 and T-2 as

$$F_i(t) = \left[\frac{u_i(t)}{u_8(t)}\right]_{\text{T-1}} - \left[\frac{u_i(t)}{u_8(t)}\right]_{\text{T-2}} \tag{3}$$

where i refers to a given measurement height (1.36, 3 or 8 m) such that F goes to zero at 8 m.

The definition given in eqn (3) differs somewhat from the classical form (as given by Schlichting [12], for example). Equation (3) is normalized to the local 8 m wind speed rather than to the "free-stream" speed, and downwind speed profiles are subtracted from the upwind profiles to account for temporal changes (nonsteady winds).

Results for Burros 8 and 9 are shown in Fig. 17. Upward displacement of the flow as a result of cold-gas intrusion is clearly evident on Burro 8 and not apparent for the higher wind conditions of Burro 9. Thus it appears that entrainment of ambient air into the cold cloud was greatly reduced on the Burro 8 test, allowing the cloud to remain relatively decoupled from the external air flow and to displace the momentum field upward. This was supported by the observation that the residence time of the cloud at the gas stations was longer than expected for simple transport at the wind speed, an effect that was also observed only on the Burro 8 test.

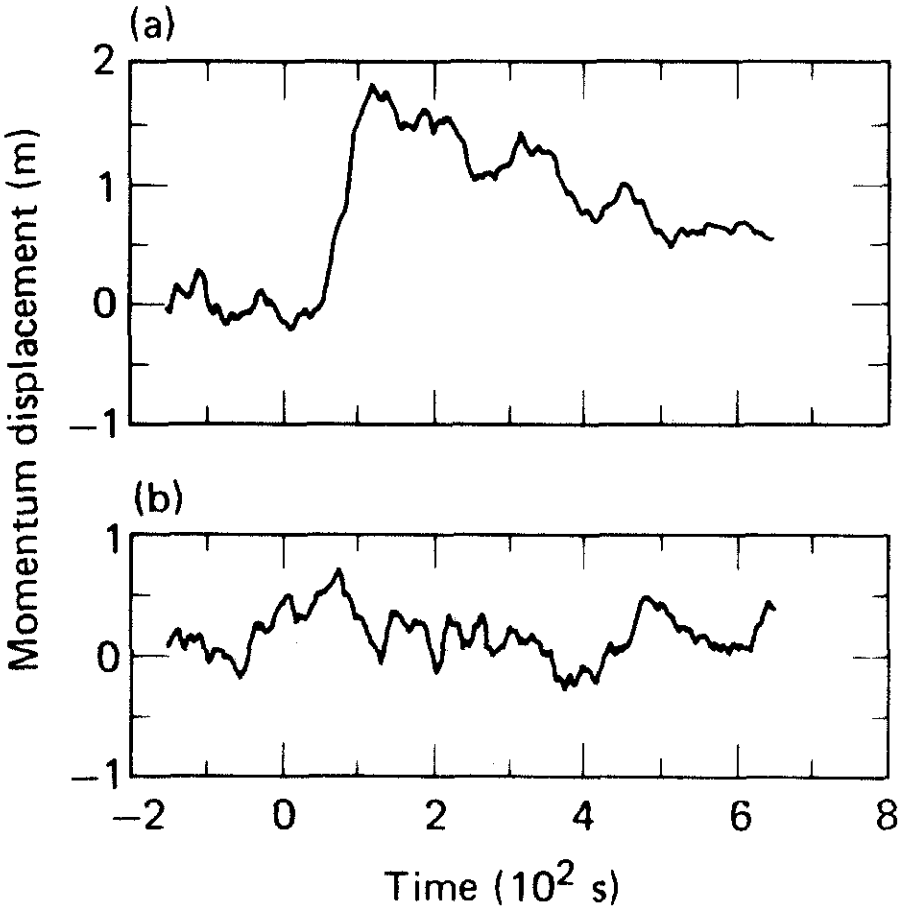

Fig. 17. Comparative momentum displacements of (a) the low-wind-speed Burro 8 and (b) higher-wind-speed Burro 9 experiments.

4.2 Surface heat flux

Measurements of heat transfer from the ground were made during passage of the cold-gas cloud, using heat-flux sensors in the ground. These sensors responded markedly to passage of the cold-gas cloud, as shown in Fig. 18. Typically, soil heat fluxes were over 200 W/m^2 when cold-gas temperatures were 15°C below ambient air at the 1 m height.

Most of the heating of the dispersing cold-gas cloud comes from adiabatic mixing of the cold gas with warm air, as well as the condensation and freezing of water vapor in the air. Previous experiments have shown that this does not account for all of the cloud heating observed experimentally and that some significant amount may come from the ground.

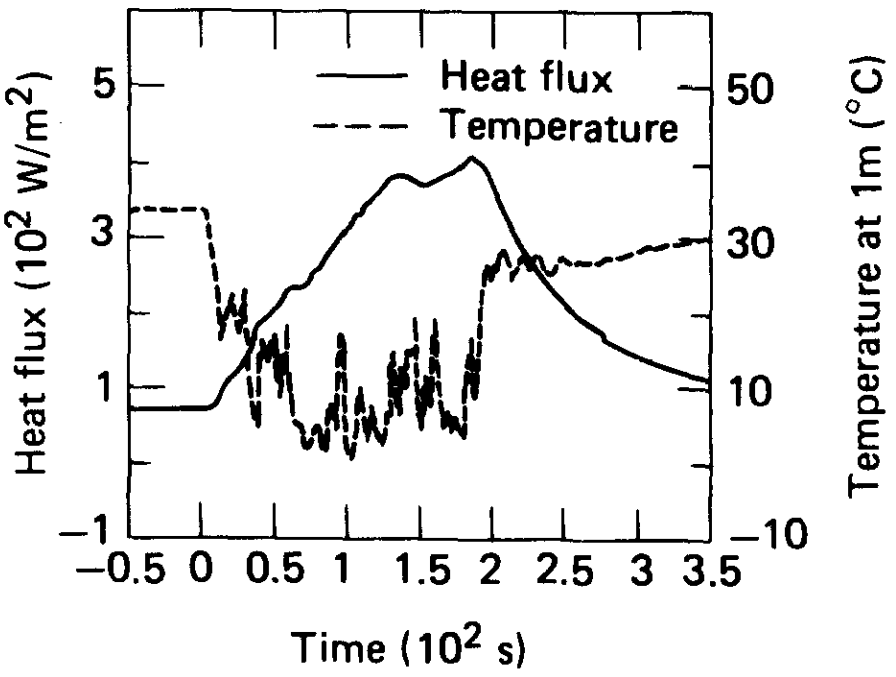

Fig. 18. Typical ground heat flux and gas temperature at 1 m height at the 57 m arc during the Burro 7 experiment.

Although a detailed energy balance analysis has not yet been performed, we investigated a simple heat-transfer model:

$$GF = V_H (\rho c_p)_{mix} \Delta T_1 \qquad (4)$$

where GF is the ground flux of heat to the gas mixture, ΔT_1 is the temperature decrease of the gas mixture at the one-metre height, V_H is a representative energy-transfer velocity (regardless of the real mechanisms of transfer), ρ is the density and c_p is the specific heat of the gas—air mixture. Since both GE and ΔT_1 change with time, this equation is representative of heat gained by the cloud only if ΔT is characteristic of the temperature difference from soil to gas, and if GF is the only significant component of heat transfer.

We found over several tests (Burro 5, 7, 8 and 9), and at both 57 and 140 m downwind, that the heat-transfer velocity V_H was apparently independent of wind speed, even when wind speed varied significantly. Investigations of more complicated models, including buoyancy terms and a drag coefficient, do not appear to be warranted by the data. As a simple approximation, the Burro test data show that V_H is nearly constant, i.e., $V_H \approx 0.0125$ m/s with a standard deviation of 36% between values from successive measurements. This model will be used in computer simulations of gas dispersion and in the energy-balance analysis now in progress.

4.3 Humidity enhancement

We investigated absolute humidity enhancement over several tests (Burros 2, 3, 5, 6, 7, 8 and 9) and at downwind distances of 57 and 140 m. Typical time traces of humidity and gas concentration at the same station are shown in Fig. 19. We found that, to a good approximation, the relative increase in absolute humidity $(\rho_w - \rho_{w_0})/\rho_{w_0}$ is correlated to gas

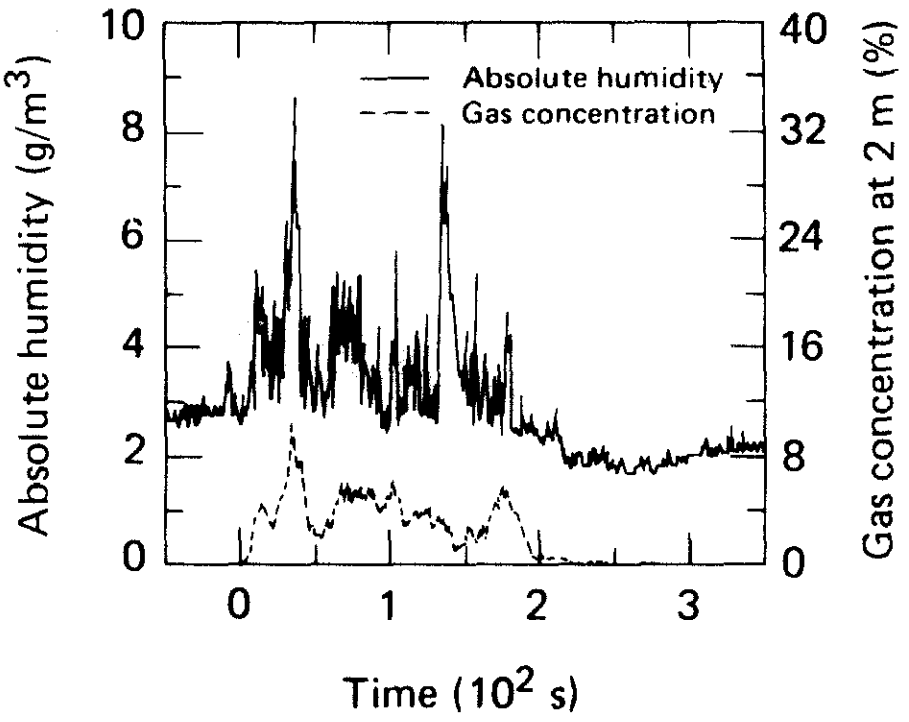

Fig. 19. Typical absolute humidity and gas concentration at 2 m height at the 57 m arc during the Burro 7 experiment.

concentration, c, in volumetric fraction, such that

$$\frac{1}{\rho_{w_0}} \frac{d\rho_w}{dc} \simeq 14.8$$

with a standard deviation of 37% between values for successive measurements. This implies that in the Burro series of tests a 1% gas concentration was associated with a 15% increase in absolute humidity. The ambient, absolute humidity values (ρ_{w_0}) averaged about 2.2 g/m^3 in the dry desert environment of the Burro tests. The humidity enhancement was negatively correlated to gas temperature also, but the variation between tests was very large. On some of the tests, air temperature remained cold long after the humidity enhancement vanished, because of the lag before ground temperatures returned to normal.

The measurement of humidity enhancement provides another element necessary to determine the overall energy balance of the dispersing cloud. Thus, the thermodynamic effects of evaporation, condensation, and subsequent re-evaporation of the additional water on the energy balance can be calculated. The relationship between humidity enhancement and the nature of the LNG spill and the extent of the cloud drift over water has not yet been determined. However, observations indicate that, under certain circumstances, humidity enhancement must be considered as a source of heat input to the cloud.

5 Differential boiling and rapid phase transitions

Strong RPT explosions were observed during the Burro 6 and 9 experi-

ments; one possible cause of these explosions is differential boiling of the LNG components. In this section, we examine the evidence for differential boiling of LNG and then review the physics of RPT explosions with respect to what was observed during the Burro series.

5.1 Differential boiling

The primary constituent of LNG is methane (~95%), with smaller fractions of ethane, propane and other heavier hydrocarbons. Although the ethane and propane concentrations are small in the liquid (4% and 1%, respectively), they are, in some respects, more hazardous than the methane since they have been shown to lower the initiation energy required to detonate mixtures of methane and air. LNG mixtures rich in ethane also exhibit a greater propensity toward RPT explosions than do those that are 95% methane, a point discussed in the following section. The nominally small fraction of heavier hydrocarbons increases substantially late in the spill due to the differential boiloff of each species according to the differences in boiling-point temperatures. The normal boiling-point temperatures for methane, ethane and propane are –161, –88 and –42°C, respectively.

Since the bulk of LNG is methane, the temperature of the liquid pool will be –161°C initially, as can be seen in the temperature-composition phase diagram for the methane-ethane system [13] shown in Fig. 20. The bulk temperature of the liquid does not increase appreciably until most of the methane has boiled off, leaving liquid rich in ethane (and propane). Consequently, high concentrations of the heavier hydrocarbons would be expected in the vapor only late in the spill.

In practically every test of the Burro series there was a noticeable increase in the ethane-plus-propane concentration at the end of the spill. This

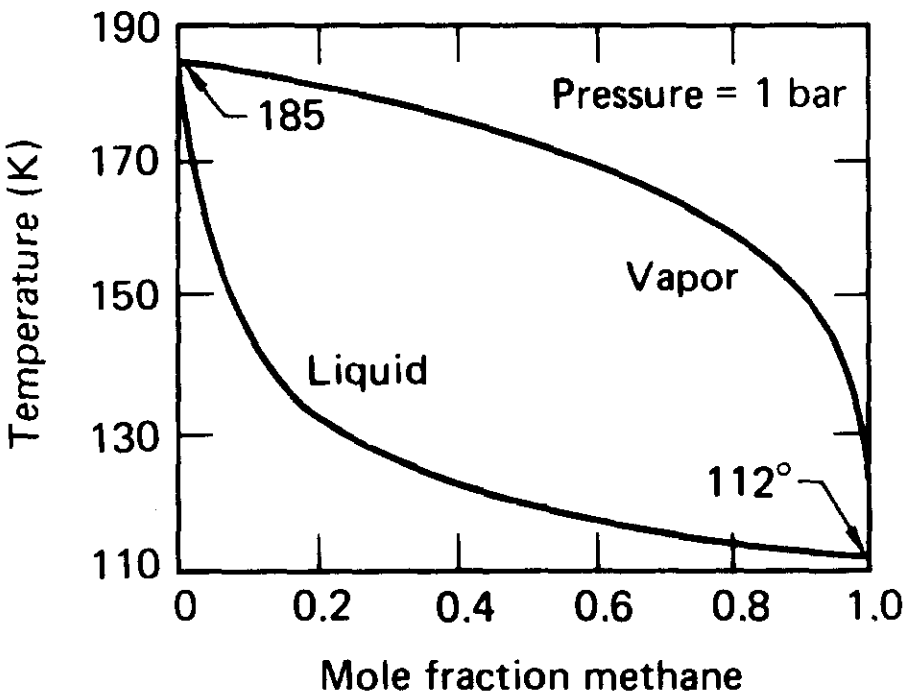

Fig. 20. Temperature—composition diagram for the methane—ethane system [13].

is illustrated by gas-concentration data from the methane and ethane-plus-propane channels shown in Fig. 21. Although this trend in the concentration data is in qualitative agreement with the expected enrichment resulting from differential boiloff, some technique for verifying the absolute values of these results is required. Verification was obtained by integrating the flux of ethane-plus-propane over the duration of the test and comparing this result to the assayed composition in the spill tank. To do this properly, the infra-red sensor being analyzed must have observed gas concentrations typical of the general cloud composition for the duration of the spill.

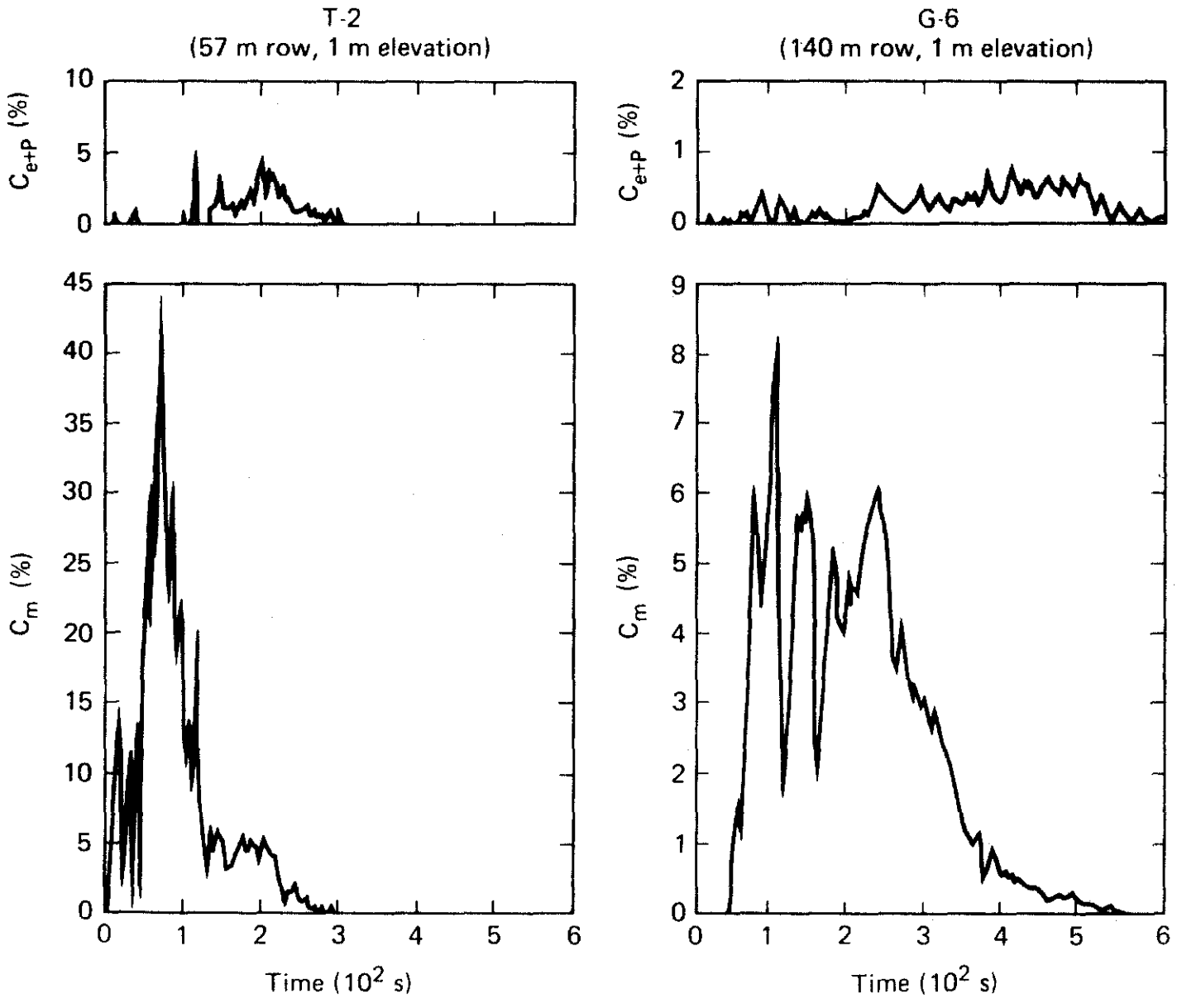

Fig. 21. Gas-concentration data for the ethane-plus-propane and methane channels from infra-red sensors in the 57 and 140 m rows for the Burro 8 experiment.

Unfortunately, the gas-concentration data from the 57 m row were generally obtained under heavy fog conditions and had to be omitted from the analysis because of the sensitivity of the ethane-plus-propane data to the fog attenuation. Imposition of these constraints on the infra-red gas-concentration data produced two sets of data appropriate for analysis. These two data sets are shown in Fig. 22 in terms of three parameters: R_0,

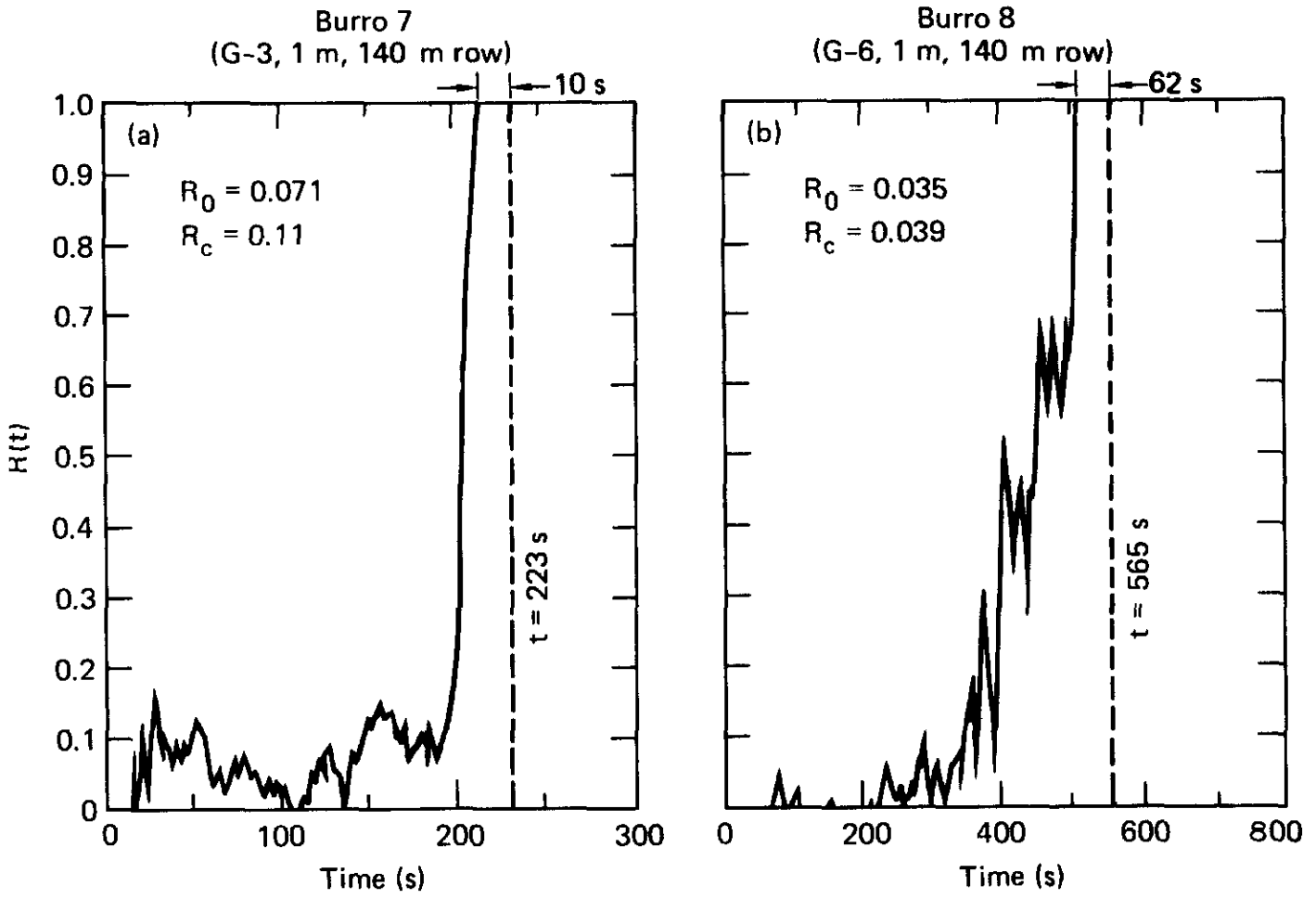

Fig. 22. Enrichment ratio vs. time for two Burro series tests.

the enrichment ratio determined from the pre-spill composition in the spill tank; R_c, the calculated vapor cloud assay; and the instantaneous enrichment ratio $R(t)$, defined as

$$R(t) = \frac{u(t)C_{e+p}(t)}{u(t)[C_{e+p}(t) + C_m(t)]} \tag{5}$$

where $u(t)$ is the wind velocity at the sensor at time t, $C_{e+p}(t)$ is the instantaneous ethane-plus-propane concentration, and $C_m(t)$ is the instantaneous methane concentration. The integral over the duration of the test of the numerator of eqn. (5) divided by the integral of the denominator of eqn. (5) is defined as R_c, i.e.,

$$R_c = \frac{\int u(t)C_{e+p}(t)\,dt}{\int u(t)[C_{e+p}(t) + C_m(t)]\,dt}. \tag{6}$$

R_0 and R_c should be equal. The results given in Fig. 22 show this to be nearly true for both Burro 7 and Burro 8.

The calculated cloud assay values (R_c) were determined by integrating eqn. (6) from $t = 0$ to the times indicated by the dashed lines on Fig. 22. These termination times correspond to the times beyond which the ethane-plus-propane concentration is less than 0.05%, a value well below the noise

level of the instrument. Consequently, the period of duration for 100% ethane-plus-propane (10 s for Burro 7 and 62 s for Burro 8) is a maximum value in both cases. The calculated assay value for Burro 7 (R_c = 0.11) is very sensitive to the choice of the integration termination time (for example, if integration is terminated at t = 213 s instead of t = 223 s, then R_c = 0.086). The calculated assay value for Burro 8 shows little variation with the choice of termination time (R_c = 0.039 for termination of t = 503 s, instead of t = 565 s). Although an accurate estimate of the extent of the enriched vapor cloud is difficult from the data in Fig. 22 because of the low concentration levels involved (less than 1%), it is evident that the effects of differential boiling on the pond were observed as far as 140 m downwind during the Burro series tests.

The measured methane and ethane-plus-propane concentrations at the center of the 57 and 140 m rows for the Burro 8 test, shown in Fig. 21, show enrichment by the heavier hydrocarbons of the later portions of the vapor at both stations, with peak ethane-plus-propane concentrations of 4% at T-2, decreasing to 1/2% at G-6. The downwind spreading or dispersion of the heavier hydrocarbons appears to be comparable to the dispersion of the methane vapors alone. This indicates that the dynamics of the dispersion of methane and ethane-plus-propane vapors are similar. The concentrations at T-2 late in the spill (t = 200 s) show that both the methane and ethane-plus-propane vapors are above the LFL and that the heavier hydrocarbons make up about 40% of the cloud at this point. In fact, the stoichiometric concentrations for a 40% ethane/60% methane mixture are 3.0% ethane, 4.5% methane and 92.5% air. Further, experiments have demonstrated [14] that just such a stoichiometric mixture can be detonated by explosive charges as small as 0.2 kg when the charges are immersed in the gas mixture. Calculations by Westbrook and Haselman [15] of a shock wave propagating through a homogeneous stoichiometric ethane, methane, and air mixture show excellent agreement with the data of Bull et al. [14] for ethane-enriched LNG vapors. Thus, it would appear that enriched LNG vapor mixtures, such as those late in the Burro 8 spill (Fig. 21), could be detonated by shock waves from explosions of sufficient magnitude. It is not known whether such a detonation in the ethane-rich region of the cloud would continue to propagate when it reached the methane-rich gas—air mixtures. It is also important to note that spill- or accident-produced clouds are not uniform in composition or well mixed, although very large clouds could have large homogeneous regions. The concentration fluctuations could also affect the propagation of the shock wave.

In considering the potential sources of initiation for such an accidental detonation in the ethane-enriched region, a disturbing new possibility arises. As will be discussed in the next section, four RPT explosions occurred on the Burro 9 test with overpressures, at 30 m, in excess of 0.18 psi (the largest being 0.72 psi). The pressure pulses observed had the characteristics of classical airblast shock waves. No data were collected during these exper-

iments to allow determination of the characteristics of the pressure pulse near the explosion source. However, if we assume the worst case and extrapolate as though the explosion were from a TNT source, we find that the shock strengths from these four explosions would be sufficient for initiation of a detonation in a stoichiometric mixture, in which the fuel is 40% ethane and 60% methane. Thus, sufficiently strong shocks may exist at the source of the RPT explosion. Furthermore, there appears to be a class of large RPT explosions, associated with differential boiloff of the LNG, that occur, preferentially, late in the spill at about the same time that the enriched region of the cloud is produced. We expect, of course, significant close-in differences between the RPT explosions and those from TNT. However, in our present analysis, we cannot discount the possibility that the shock wave produced by an RPT could ignite the ethane-rich portion of an LNG vapor cloud. Close-in shock pressure and vapor-composition measurements will be necessary to resolve this issue.

5.2 Burro series rapid phase transition (RPT) explosions

Numerous RPT explosions occurred with varying severity and frequency during two of the Burro series spills in 1980. A summary of all available data pertinent to RPT explosions for the Burro series spills is given in Table 2. Several large explosions occurred during the Burro 6 and 9 spills. Examination of Table 2 shows that many variables are involved: pressurization technique, spill rate, spill-plate location, LNG composition, and the time of occurrence of the RPT explosions. Unfortunately, these variables were not controlled; as a result, one cannot deduce the precise cause of the RPT explosions. Clearly the heavy hydrocarbon concentrations, as measured in the tank shortly before each spill, are much lower than the 60% minimum required to produce simple spill RPT explosions according to Porteous [16]. Also, the estimated impact velocity associated with the maximum spill rate obtained (Burro 9) was less than 5 m/s (assuming liquid phase only) — well below the range of impact velocities for which the RPT's were observed at M.I.T. [17].

There were several large RPT explosions very late (~130 s) in the Burro 6 spill. These explosions occurred in rapid succession and out on the pond, away from the spill point. In this case, we believe that the explosions were the result of the enrichment of the LNG caused by the differential boiloff of the methane on the pond. It is not yet apparent why this happened during Burro 6 and not during Burros 2—5, since the spill rates and tank compositions for the five spills were similar. The only obvious difference was that Burro 6 involved partial self-pressurization and may have had less dissolved nitrogen present. However, the nitrogen should have come out of solution very early in the spill and not affected the pool characteristics at the times of the RPT explosions.

The spill plate that was attached to the spill-pipe exit also complicated analysis of the RPT explosions. Although the spill plate was submerged in

TABLE 2

Burro-series RPT explosion summary

Experiment	RPT	Time of occurrence	Ambient temperature (°C)	Self-pressurization	Average spill rate (m^3/min)	Spill-plate location	LNG composition (%)		
							CH_4	C_2H_6	C_3H_8
2			37.6	No	11.9	About 5 cm below water	91.3	7.2	1.5
3			33.8	No	12.2	About 5 cm below water	92.5	6.2	1.3
4			35.3	No	12.1	Below water	93.3	5.1	1.1
5			40.5	No	11.3	Water level	93.6	5.3	1.1
6	Several large	Late in spill	39.2	Yes	12.8	?	92.8	5.8	1.4
7			33.7	Yes	13.6	Above water	87	10.4	2.6
8			33.1	Yes	16.0	Above water	87.4	10.3	2.3
9	Numerous very large	Throughout entire spill	35.4	Yes	18.4	About 5 cm below water	83.1	13.9	3.0

the early tests (Burros 2 and 3), allowing the LNG to come into initial contact with the water, the spill rate was lower, resulting in a smaller impact pressure. As the spill rate increased (Burros 6—9), little (if any) water was available for the initial direct impact of the LNG until Burro 9. This was caused by evaporation and the resultant lowering of the pond water level, which customarily occurs each summer. Before the Burro 9 spill, the spill plate was lowered about 5 cm below the surface of the water, allowing LNG spilled at the maximum spill rate to interact more readily with the water. Unfortunately, there were other differences between the Burro 9 spill and the previous ones: an unusual cooldown and the loss of the spill plate during the spill.

The typical Burro series cooldown procedure was as follows. Several hours before the estimated spill time, the test director would begin to cool down the portion of the spill pipe up to the spill valve (see Fig. 1). This was accomplished by closing the tank vent valve and allowing the tank to partially self-pressurize by evaporation, forcing the LNG up the dip tube, where it spilled over into the 53-m-long section of pipe leading to the spill valve. The pipe vent valve allowed vaporized gases in this pipe section to escape so that the entire volume (2.2 m^3) could be filled with LNG. Dr. C.D. Lind of the Naval Weapons Center, the test director, estimates that the methane concentration in this section of the spill pipe could be no less than 85% as a result of the preferential methane evaporation. This self-pressurization scheme produced pressures of about 5 psi in the tank 15 min before the test. The pressure was then boosted slowly to 30 psi, using compressed nitrogen. During the cooldown procedure the bypass valve was partially opened, and some LNG was allowed to trickle out the remaining 41 m of the spill pipe in an attempt to cool this pipe section. The LNG in this last section of the spill pipe was surely further enriched in the heavier hydrocarbons; however, an accurate estimate of the degree of enrichment is difficult.

During Burro 9 cooldown the bypass valve malfunctioned, allowing a larger than normal flow of LNG out the spill pipe before the spill. Consequently, an abnormally large amount of enriched LNG may have been in the spill pipe when the spill valve was opened. Perhaps the pressure wave generated when the spill valve first opened forced the enriched LNG in the last 41-m-long section of the spill pipe out the exhaust ahead of the main body of LNG and produced the first few RPT explosions. This scenario is substantiated somewhat by the timing of the RPT explosions and by the flow-rate data obtained just upstream of the spill valve. Using the flowrate data and assuming single-phase (liquid) flow for the duration of the spill, a simple calculation shows that at least 10 s would be required for the LNG on the upstream side of the spill valve to reach the pond surface. As shown in Table 3, there were three RPT explosions before this. The second largest explosion occurred at 21.4 s when the LNG initially in the 53-m-long section of the spill pipe was being exhausted, and the storage-tank LNG was spilling out when the largest RPT explosion occurred at 35.1 s. This would

TABLE 3

Occurrence times and magnitudes of major Burro 9 RPT explosions [18]

Time [a] (s)	Static pressure [b] (psi)	TNT equivalent [c] (g)
6.5	0.12	65
7.1	0.15	115
9.2	0.27	530
21.4	0.57	3400
35.1	0.72	6300
43.2	0.10	41
46.0	0.12	65
54.1	0.12	65
54.9	0.13	80
66.9	0.19	215
72.7	0.12	65

[a] $t = 0$ is start of spill-valve opening.
[b] Measured at distance of 30 m.
[c] Equivalent free-air point-source explosion of TNT.

seem to indicate that LNG containing only 17% heavier hydrocarbons and impacting at velocities of less than 7 m/s (assuming single-phase flow) can produce significant RPT explosions. One must also consider that the spill plate was knocked loose some time before the largest explosion (35.1 s), greatly changing the LNG—water interaction dynamics. The exact time of this occurrence and its effect on the RPT explosions is not known.

Lind recorded 20 significant RPT explosions during the Burro 9 spill [18]. The largest 11 and their times of occurrence are given in Table 3. Films show that large airblast overpressures are not necessarily associated with large water-plumes, indicating that some of the explosions occurred deep (1 m) underwater. Damage to the facility also indicates that large explosions must have occurred essentially at the pond bottom. Analysis of the airblast measurements indicates that at least 50 MJ of energy was released in the 20 explosions, which corresponds to 11 kg of TNT. The polymorphic detonation theory developed at Washington State University [19,20] allows one to estimate the minimum amount of superheated cryogen needed to produce a detonation of known magnitude. The theory employs the volume change of the phase transformation as the energy required to sustain a detonation wave, and the superheat phenomenon as the energy-storage mechanism. The initial work by Rabie et al. [19] was extended by Hixson [20] to describe detonation properties based on more realistic equations of state. However, the equations are involved and, as yet, have only been used to calculate the bounds of the detonation properties for methane and propane. If the fluid is heated to the superheat temperature limit at 1 atm, the energy available for detonation is about 83 J/g for methane and 112 J/g

for propane. The minimum volumes of methane, ethane and propane necessary to produce the energy release measured during the Burro 9 RPT explosions are 1.46, 0.93 and 0.79 m^3, respectively. This is certainly a lower limit since the attenuation of the blast waves from the underwater explosions was not accounted for. The actual volumes spilled were 22.66, 1.26 and 0.23 m^3, respectively. The required volume of ethane was calculated, using an estimated available detonation energy of 100 J/g. Clearly, only a small fraction of the methane would have to be superheated, whereas practically the entire spilled volumes of ethane and propane would have to be heated to the superheat limit at the same moment to produce the measured explosive energy release. Thus, it is clear that significant amounts of methane must have contributed to these RPT's. This is further evidence that a standard mixture of LNG (80—90% methane) spilled onto the water at low velocity is capable of undergoing significant RPT explosions.

At this time, we can only make general conclusions about the RPT explosions during the Burro series. The late explosions of Burro 6 were most likely caused by enrichment of the LNG pool as a result of the differential boil-off of the methane. However, it is very difficult to draw any conclusions about the Burro 9 RPT explosions because of the lack of quantitative information on the pertinent parameters. The pressure measurements — fielded by Lind after the initial RPT occurrence on Burro 6 — produced very useful data during the Burro 9 RPT's, but not enough data were obtained to understand the mechanism or to predict what might happen during an accident.

Summary and conclusions

Of the eight Burro series LNG spill experiments performed at China Lake in 1980, four proved to be identifiably different from each other and amenable to analysis. The Burro 3 test was performed in an unstable atmosphere, with a moderate wind speed and a low spill rate. Burro 7 had a low spill rate, high wind speed, and slightly unstable atmosphere. The Burro 8 test was particularly interesting in that it had a high spill rate, very low wind speed, and slightly stable atmosphere. Burro 9 had the highest spill rate of all, moderate wind speed, neutral atmospheric stability, and numerous RPT's. Most of our analysis has been centered on these four tests.

An extensive array of instrumentation was deployed both upwind and downwind of the spill pond. Wind speed and direction, humidity and temperature were measured both upwind and downwind. Four radial arcs containing 30 gas-sensor stations were deployed downwind to 880 m from the spill pond and measured gas concentration and temperature at three elevations, as well as humidity and heat flux from the ground.

The gas-concentration and wind-field data were processed and analyzed to define the gas cloud as a function of time using contour plots, and the wind field as a function of time using wind-field flow lines. The gas cloud

orientation and the wind-field flow lines were generally consistent in that the maximum gas concentrations generally lay along the wind-field centerline. The notable exception to this was Burro 8 in which the gas flow was dominated by gravity, producing a highly bifurcated cloud that tended to follow low regions of the terrain. The bifurcated cloud caused maximum gas concentrations to occur on either side of the wind-field centerline. Other exceptions occurred when the cloud extended beyond one side of the array where the extrapolated wind field was not reliable or when several gas sensors were not operational, causing distortions in the gas contours.

Additional consistency checks were made in an attempt to demonstrate the validity of the data. The mass flux of gas through an arc of gas sensors (140 m arc) was calculated and integrated over the duration of the test for both Burro 8 and 9). The cloud stayed within the array for Burro 9 and, if RPT effects are considered, the gas sensors accounted for essentially all of the LNG spilled. The gas cloud from Burro 8 was visibly wider than the instrument array, but the mass-balance calculation indicates that 76% of the gas was detected. The mass flux of ethane-plus-propane was also calculated and integrated over the spill duration. The results compared favorably with the tank assays at the time of the tests.

The normal turbulent flow in the lower atmospheric boundary layer totally dominated the transport and dispersion of gas on all of the tests except Burro 8. On this test, the wind speed was low and the gas flow was dominated by gravity. This produced an exceptionally wide low cloud that actually displaced the ambient wind field upward by about 1.5 m, causing the wind speed within the cloud to drop essentially to zero. We believe that what was observed to occur during Burro 8, under very low wind conditions, is likely to occur on larger spills under a variety of conditions. The ability of large masses of cold, dense gas to displace the normal atmospheric flow has profound implications for hazard prediction from large accidental spills. Larger spills are badly needed to determine if this phenomena is likely to be important in the case of an accident.

Time histories of the downwind distance to the LFL were obtained from the gas-concentration contours for Burros 3 and 7—9. The downwind LFL location appeared to stabilize only in the case of Burro 8, where it was 330 m at a height of 1 m. However, the occurrence of 5% gas concentrations at a height of 3 m at the outermost stations in the 400 m arc, late in the Burro 8 test, indicate that the furthest extent of the LFL may have been missed.

Large-scale differential boiloff of the various constituents of the LNG was again observed on this series of tests. Substantial ethane and propane enrichment of the cloud occurred late in the spills and propagated downwind. Flammable mixtures with enrichments of the fuel ranging up to 40% ethane and propane were observed to travel downwind substantially beyond the 57 m arc, reaching the 140 m arc in some cases. This ethane-enriched region represents an additional hazard since it is more easily detonated than the methane-rich majority of the cloud.

Data and theory available before the Burro series indicated that RPT explosions were not likely to occur. Although numerous explosions were observed on both Burros 6 and 9, they occurred under very different circumstances. Differential boiling and the consequent enrichment in higher hydrocarbons of the LNG appear to be involved in the Burro 6 explosions, but the Burro 9 explosions appear to be due substantially to the direct interaction of LNG with water. The explosions were energetic enough to have caused some damage to the facility, with a maximum overpressure (static) of 0.72 psi being recorded at 30 m. Two disturbing possibilities associated with the occurrence of RPT's arise: first, RPT's could be energetic enough to turn a small accident into a large one and, second, the RPT-produced shockwave might be energetic enough to ignite the ethane-rich and more easily detonatable region of the vapor cloud. More large experiments at higher spill velocities will be required to determine how severe these hazards might be.

The high-frequency data (3—5 Hz) indicate significant fluctuations about the 10-s-average values used as the basis for discussions of gas-transport and generation of contour plots. Fluctuations above 5% gas concentration are commonly associated with 10-s mean concentrations above 1%. This implies that the flammable extent of a gas cloud will be larger than is indicated by the mean LFL contour generated from either the experimental data or computer calculations.

The heat flux from the ground into the cold cloud was found to be independent of wind speed. Although several more complicated models were tried, the data correlate best with a simple linear dependence on temperature difference between the ground and the cloud.

Humidity measurements made both upwind and downwind in the array indicated that the water content of the gas cloud was substantially higher than the ambient air. The correlation showed that a 1% gas concentration was associated with a 15% increase in absolute humidity. The mechanism by which this additional water is entrained by the cloud during the spill process is not yet known. However, both humidity and heat flux contribute to the overall energy balance of the dispersing gas cloud and can affect the nature of the dispersion.

The data discussed in this paper are part of the ongoing DOE program of safety research into liquefied gaseous fuels. The goal of the program is to be able to predict the hazards associated with accidents involving LNG or other liquefied gaseous fuels. To that end, the data are being used for detailed comparisons with computer models, but it is clear that we do not have enough information on hand to draw general conclusions about the effects of varying atmospheric and spill conditions. The Burro 8 data have demonstrated to us that larger tests are necessary if the relationship between spill size and atmospheric dispersion is to be understood. Additional field experiments to investigate RPT's and vapor fires are currently underway, as is further analysis of the data and comparison with theory and models.

Acknowledgments

This paper is based on the efforts of many others who contributed to the success of the experiment and the data analysis. While we cannot mention them all, we would like to single out a few for special thanks. First and foremost are Lyle Kamppinen, Rod Kiefer, John Baker, Troy Williams and Miles Spann of the LLNL Electrical Engineering Department and the crew of electronics technicians from both LLNL and the EG & G Special Measurements Department, without whose dedication, innovation and technical excellence this work would not have been possible.

We would also like to acknowledge the contribution of Bill Wakeman, Greg Bianchi, Rex Blocker and the other mechanical engineers and technicians who helped with the field work. Our special thanks go to Louise Morris who generated the gas-concentration contours, to Don Baltz and other members of the EG & G Scientific Services Department who did much of the data-acquisition-system programming, to Bill Ginsberg and other members of the EG & G Remote Measurements Department who did helicopter-based infra-red imaging of the tests, and to Jeff Simmonds and his group from the Jet Propulsion Laboratory who built and fielded the FBDR infra-red gas sensor.

This work is also the direct result of capable and supportive program leadership. We would like to acknowledge John Cece, our DOE contract monitor, Bill Hogan, our LLNL LGF Program Leader, and Doug Lind, the leader of the NWC team, for their help in making these experiments a success.

References

1 R.P. Koopman, L.M. Kamppinen, W.J. Hogan and C.D. Lind, Burro series data report: LLNL/NWC 1980 LNG spill tests, Lawrence Livermore Nat. Lab., Livermore, CA, UCID-19075, 1981.

2 G.E. Bingham, R.D. Kiefer, C.H. Gillespie, T.G. McRae, H.C. Goldwire and R.P. Koopman, A portable, fast-response multiwavelength infra-red sensor for methane and ethane in the presence of heavy fog, Lawrence Livermore Nat. Lab., Livermore, CA, UCRL-84850, 1980.

3 J.M. Conley, J.J. Simmonds, R.A. Britten and M. Sinna, A four-band differential radiometer for monitoring LNG vapors in liquefied gaseous fuels safety and environmental control assessment program: second status report, U.S. Dept. of Energy, DOE/EV-0085, Report L, 1980.

4 P. Dubois, J. Fletcher and M. Richards, Livermore time-sharing system: Chap. 4, Files, edn. 2, Rev. 1, Computer Information Center, Lawrence Livermore Nat. Lab., Livermore, CA, CIC LTSS-4, 1976.

5 S.E. Jones and D.R. Ries, A relational data-base management system for scientific data, Lawrence Livermore Nat. Lab., Livermore, CA, UCRL-80769, 1978.

6 G. Peterson and A.B. Budgor, The computer language MATHSY and applications to solid state physics, Comm. ACM, 23 (1980) 466.

7 C.A. Paulsen, The mathematical representation of wind speed and temperature profiles in the unstable atmospheric surface layer, J. App. Meteor., 9 (1970) 857.

8 A.J. Dyer, A review of flux-profile relationships, Boundary-Layer Meteorol., 7 (1974) 363.
9 H.H. Lettau, Wind and temperature profile prediction for diabatic surface layers including strong inversion cases, Boundary-Layer Meteorol., 17 (1979) 443.
10 D.L. Ermak, R.A. Nyholm and R. Lange, ATMAS: a three-dimensional atmospheric transport model to treat multiple area sources, Lawrence Livermore Nat. Lab., Livermore, CA, UCRL-52603, 1978.
11 G.T. Csanady, Turbulent Diffusion in the Environment, D. Reidel Publishing Co., Dordrecht, The Netherlands, 1973, pp. 145 and 225.
12 H. Schlichting, Boundary Layer Theory, McGraw-Hill, New York, 4th edn., 1960, p. 27.
13 J.A. Valencia-Chavez and R.C. Reid, The effect of composition on the boiling rates of liquefied natural gas for confined spills on water, Int. J. Heat Mass Transfer, 22 (1979) 831—838.
14 D.C. Bull, J.E. Ellsworth and G. Hooper, Initiation of spherical detonation in hydrocarbon/air mixtures, presented at the Sixth Int. Coll. on Gasdynamics of Explosions and Reactive Systems, Stockholm, Sweden, 1977, Acta Astr., 5 (1978) 997.
15 C.K. Westbrook and L.C. Haselman, Chemical kinetics in LNG detonations, Liquefied gaseous fuels safety and environmental control assessment program: second status report, U.S. Dept. of Energy, DOE/EV-0085, Report F, 1980.
16 W.M. Porteous, Super heating and cryogenic vapor explosions, PhD thesis, Massachusetts Institute of Technology, Cambridge, MA, 1975.
17 B. Jazayeri, Impact cryogenic vapor explosions, MS thesis, Massachusetts Institute of Technology, Cambridge, MA, 1975.
18 C.D. Lind, Naval Weapon Center, China Lake, CA, Personal communication, 1980.
19 R.L. Rabie, G.R. Fowles and W. Fickett, The polymorphic detonation, Phys. Fluids, 22 (1979) 422.
20 R.S. Hixson, Vapor phase detonations in light hydrocarbons, PhD thesis, Washington State University, Pullman, WA, 1980.